Ad Hoc Networks 179 (2025) 104019

Contents lists available at ScienceDirect

Ad Hoc Networks

journal homepage: www.elsevier.com/locate/adhoc

Quantify the joint effect of mobility and urban environment on computation offloading to multi-UAV MEC network: Sojourn time

Basheer Ameen Raddwan [a,*], Ibrahim Ahmed Al-Baltah [a,b]

[a] Department of Information Technology, Faculty of Computer Science and IT, Sana'a University, Sana'a, Yemen
[b] Department of Information Technology, Faculty of Science and Engineering, Al-Hikma University, Sana'a, Yemen

ARTICLE INFO

Dataset link: UAV Mobility Tracing in 72 Urban Environments (Original data)

Keywords:
Unmanned aerial vehicles
Mobility
Multi-access edge computing
Sojourn time
Computation offloading
Urban

ABSTRACT

The integration of Multi-Access or Mobile Edge Computing (MEC) with Unmanned Aerial Vehicles (UAVs) offers transformative prospects for 5G/6G networks, especially with compute offloading in urban settings. The combined effect of the mobility of airborne MECs (airMECs) and urban environmental dynamics has not been explored in current research, which has shown that the optimization strategy may be impractical in densely populated areas due to the restricted computational resources available on airMECs. In this paper, we analyze the combined mobility of users and airMECs while considering urban dynamics constraints to quantify sojourn time, which serves as a valuable input for mobility characterization in planning. We introduce novel analytical and statistical approaches to quantify sojourn time for both omnidirectional and directional antenna scenarios. We develop the statistical approach by simulating three-dimensional mobility in numerous urban configurations and gather ray-tracing line-of-sight data for two scenarios. The first scenario excludes buildings to verify the statistical approach against the analytical one, whereas the second scenario includes buildings to assess their influence. Following the quantification of the suggested environment-dependent sojourn time, we present a stochastic task size quantification as an application example. Additionally, we present many evaluations to ensure the accuracy and the practicality of the proposed models. For example, we analyze the circular directionality of sojourn time using the Von Mises probability distribution, examining task sizes with offloading time, and assessing handover times for a designated task size. The findings indicate that environmental dynamics significantly influence sojourn time and computational offloading, necessitating explicit consideration in airMEC network planning and MEC application design. This study offers critical insights for developing resilient, adaptive networks that support computation-intensive applications in dynamic urban environments.

1. Introduction

The swift progress of modern network services, such as augmented reality, autonomous vehicles, and service robots, has led to a considerable demand for bandwidth and computational offloading to cloud computing. Recent advancements in technologies such as Intelligent Reflective Surfaces [1], Ultra-Dense Networks [2], and Multi-Access Edge Computing [3,4] have been introduced to enhance network performance and meet the latency demands of emerging services. Moreover, Unmanned Aerial Vehicles (UAVs) are proposed to support Multi-access or Mobile Edge Computing (MEC) systems (airMECs) in reducing computational offloading latency in densely populated regions [5,6], leveraging UAVs' agile maneuverability, autonomous flight, and low operational expenses.

Despite the advantages of using airMECs to host compute offloading services, this paradigm has also presented further challenges. The constrained computational resources of airMECs constitute a significant limitation, especially for large task sizes in densely populated regions. Recent studies demonstrate that offloading latency increases with larger task sizes [7,8], and more users [9–11]. The analytical solution presented in [12] indicates that controlling velocity to extend sojourn time is inadequate for reducing offloading latency. This strategy results in a higher number of users within the serving area of the MECs, thereby increasing the consumption of computational resources. Recent research emphasizes trajectory optimization to improve user sojourn times by positioning serving airMECs in proximity to users.

Moreover, current research has neglected urban environmental dynamics, such as building and street dimensions, which influence line-of-sight (LoS) conditions between users and airMECs and compel street-like movement patterns. Simple mobility patterns and trace-based mobility have been studied or introduced to trajectory management. Basic

* Corresponding author.
E-mail address: basheer@su.edu.ye (B.A. Raddwan).

https://doi.org/10.1016/j.adhoc.2025.104019
Received 31 March 2025; Received in revised form 19 August 2025; Accepted 4 September 2025
Available online 12 September 2025
1570-8705/© 2025 Elsevier B.V. All rights are reserved, including those for text and data mining, AI training, and similar technologies.

mobility models inadequately account for movement in urban environments, and trace-based datasets are scarce globally due to privacy concerns and the high costs associated with data collection. Similarly, existing literature has not incorporated sojourn time into optimization methods and lacks a characterization of mobility within urban environments.

This paper addresses the aforementioned limitations and presents an innovative approach for analyzing 3D mobility across various urban environment configurations. We examine mobility for both users and airMECs, emphasizing the necessity for moving entities to adhere to street grids and evade collisions with buildings and other mobile objects. We simulate 3D mobility in a large number of urban settings to gather data on ray-tracing LoS, mobility positions, and orientations of mobile objects. We statistically formulate the sojourn time models based on the collected synthetic trace-based mobility. Finally, we employ the resulting sojourn time to quantify environment-dependent task size. The main contributions of the paper are summarized as follows.

1. This study presents a new circular representation of urban environments designed to encompass various urban settings within the interval $[-\pi, \pi]$. This approach enhances the analysis and visualization of environmental impacts on metrics, including offloading latency and task sizes.
2. To characterize sojourn time in the airMEC context, we developed novel analytical and statistical approaches. The analytical sojourn time is determined by the elliptical configuration of the directional antenna's coverage footprint on the ground, and it is solved numerically using the complete elliptic integral of the second kind. Due to the complexity of mathematically accounting for large structure blockage of LoS, we use a game-based technique to gather ray-tracing LoS data to formulate the statistical sojourn time. Owing to the different coverage footprint and signal strength of omnidirectional versus directional antennas, we concurrently collect LoS data for both types. We simulate the same urban settings and the same mobility patterns in two scenarios. The first scenario does not include buildings, allowing us to validate the statistical approach against the mathematical one. We use buildings in the second scenario to evaluate their impact on the statistical approach.
3. We visually inspect the resulting statistical sojourn time models, observing that peaks of sojourn times exhibit varying orientations when comparing the omnidirectional and the directional antenna scenarios. We conduct a directionality analysis using the Von Mises probability distribution to characterize the stochastic nature of the environmental impact.
4. To address the application dimensioning in the design phase of the airMEC networks, we introduce a novel task sizing method that stochastically quantifies the maximum offloadable task size during the mean sojourn time intervals in urban settings. We present two environment-dependent task sizes for both omnidirectional and directional scenarios as cubic polynomials. We also analyze the environmental impact on handover times for specific task sizes in both scenarios.

We organize the remainder of this article as follows: The related work of task offloading to terrestrial and airborne MECs is briefly reviewed, focusing on mobility and environmental perspectives in Section 2. The system model is explained in Section 3, which includes models for the network, the urban environment, the analytical sojourn time, and task offloading. Section 4 discusses the core methodology, while the complexity analysis is described in Section 5. The experimental setup, results, and discussions are presented in Section 6. Finally, the conclusion and future research opportunities are stated in Section 7.

2. Related work

2.1. Offloading to terrestrial MECs

Extensive research has been conducted on mobility-aware computation offloading to terrestrial MEC systems situated near wireless access points, emphasizing optimization challenges addressed through heuristic, evolutionary, and learning-based methodologies. A heuristic software-defined networking load-balancing scheme is presented in [13] to improve the efficiency of computational resource utilization. The research presented in [14] proposes a clustering-assisted offloading scheme based on affinity propagation to reduce the frequency of service migration. Furthermore, the application of non-orthogonal multiple access (NOMA) technology is presented to improve computation offloading latency [8,15]. A joint optimization of resource allocation and offloading latency is proposed in [15], while a distributed evolutionary algorithm is introduced in [8] to optimize task offloading latency and energy consumption in vehicular networks.

Learning-based solutions have emerged as effective methods for long-term optimization. The study in [16] examines computation offloading from a user terminal to an MEC directly or via a relay from a nearby user terminal, utilizing a device-to-device interface determined by the serving base station. This study utilizes deep learning techniques for trajectory prediction of the gUT sojourn time, derived from pedestrian movements on the Stanford University campus as documented in the Stanford Drone Dataset. The study in [17] introduces a genetic algorithm aimed at jointly optimizing federated learning and computation offloading in vehicular networks, utilizing high-altitude platforms to support terrestrial MEC. Federated learning posits that both MEC and the user exchange information and participate in the decision-making process. A deep deterministic policy gradient-based greedy algorithm (IDDPG-GA) is proposed for ultra-dense networks to jointly optimize dynamic offloading and resource allocation, as outlined in [2]. Another federated learning is proposed in [18] to minimize latency. Additionally, joint energy consumption and offloading latency are optimized through a DRL-based group relative policy solution in [11] for mobile IoT networks. Heuristic and deep reinforcement learning is proposed in [19] to enhance security for workflow applications in cyber–physical systems.

2.2. Offloading to AirMECs

The airMECs represent a promising approach to improving the performance of MEC systems, characterized by their flexible and agile deployment, extensive coverage, and dependable wireless communication. Research on computation offloading to airMEC systems has been conducted during the operational phase, focusing on both traditional and learning-based optimization techniques. An evolutionary trajectory planning algorithm is introduced in [20] aimed at minimizing UAV energy consumption within IoT networks. A joint optimization algorithm for UAV trajectory and resource allocation is presented in [21]. The research presented in [22] proposes a joint optimization of UAV trajectory and offloading delay, utilizing a trace-based user mobility model. The block alternating descent method optimizes computational resource allocation in the UAV trajectory, as discussed in [23], while in [24], a genetic trajectory planning method with variable population size is proposed to minimize cumulative hovering and flying energy for UAVs.

Studies based on learning have concentrated on trajectory planning or determining UAV positioning to meet optimization objectives. The study in [25] introduces a DLR-based approach for the simultaneous optimization of a single UAV trajectory and task offloading scheduling. The research presented in [26] proposes a distributed deep reinforcement learning (DDRL) framework that integrates cooperative exploration and prioritized experience replay (PER) for managing UAV mobility patterns while considering task offloading and UAV

Table 1
Comparison with existing mobility-aware research.

Reference	MEC type	User type	Multi-UAV	Dimension	Environment	User mobility pattern	UAV mobility pattern	Mobility impact metric	Task size
[21]	AirMEC	IoTs	✓	3D	ITU-R P.1410	Fixed	Trajectory	NA	Small
[14]	MEC	gUTs	NA	2D	NA	Trajectory	NA	NA	NA
[16]	MEC	gUTs	NA	2D	NA	Trace-based	NA	Sojourn time	Small
[22]	AirMEC	gUTs	✓	3D	ITU-R P.1410	Trace-based	Trajectory	NA	Small
[25]	AirMEC	gUTs	×	3D	ITU-R P.1410	Fixed	Trajectory	NA	Large
[23]	AirMEC	gUTs	×	2D	NA	Fixed	Trajectory	NA	Large
[26]	AirMEC	gUTs	✓	2D	NA	Fixed	Trajectory	NA	Small
[27]	AirMEC	gUTs	✓	3D	Generic urban	Fixed	Trajectory	NA	Small
[24]	AirMEC	gUTs	✓	2D	NA	Fixed	Trajectory	NA	Large
[17]	MEC, HAP	vUTs	NA	2D	Two-lane road	Straight line	NA	Sojourn time	Small
[12]	MEC	vUTs	NA	2D	Highway	Straight line	NA	Sojourn time	Small
[15]	MEC	vUTs	NA	2D	One-lane road	Straight line	NA	Sojourn time	Small
[9]	AirMEC	vUTs	✓	2D	NA	Fixed	Follow vehicle	NA	NA
[7]	AirMEC	IoTs	×	2D	Generic urban	Fixed	Trajectory	NA	Large
[28]	AirMEC	gUTs	✓	2D	Generic urban	Fixed	Trajectory	NA	Small
[18]	MEC	gUTs	NA	NA	Urban roads	Trace-based	NA	NA	Small
[10]	AirMEC	gUTs	✓	2D	NA	Fixed	Trajectory	NA	Small
[2]	MEC	gUTs	NA	2D	NA	Trajectory	NA	NA	Small
[11]	MEC	IoTs	NA	2D	NA	Grouped	NA	NA	Small
[8]	MEC	vUTs	NA	2D	Urban roads	Straight line	NA	NA	Small
This article	AirMEC	gUTs	✓	3D	ITU-R P.1410	Controlled	Controlled	Sojourn time	Large

failure constraints. The research presented in [27] focuses on minimizing energy consumption for UEs and UAVs through the optimization of offloading delay, MIMO channel, transmission power, and UAV positioning. The research has introduced two solutions. The first approach employs a genetic-based heuristic for joint power and quality of experience, whereas the second utilizes a deep deterministic policy gradient (DDPG) algorithm. The research in [9] introduces a mobility-aware strategy for service offloading and migration in the context of the Internet of Vehicles (IoV). The research implements a two-step optimization strategy that incorporates Lyapunov optimization alongside the multi-agent deep deterministic policy gradient (MADDPG) technique to minimize task offloading latency while conforming to a defined long-term migration cost constraint. In [7], a Markov decision process is developed to simultaneously enhance trajectory and task offloading latency by employing a long short-term memory (LSTM) network combined with an attention mechanism and a deep deterministic policy gradient (DDPG) algorithm. The research presented in [28] develops a multi-agent Markov decision process (MDP) and introduces a multi-agent proximal policy optimization framework utilizing a beta distribution to concurrently optimize UAV trajectory, task partitioning, and resource allocation. The study in [10] proposes a collaboration between a multi-agent deep deterministic policy gradient and a distance-to-task location and capability match algorithm to optimize UAV trajectory, task offloading decisions, and resource allocation. The study in [29] introduces trajectory-based task offloading optimization using DRL with MDP.

2.3. Mobility effect in urban environment: Sojourn time

The literature recognizes mobility as a significant challenge in optimizing computational offloading in MEC-enabled next-generation networks. This section reviews various mobility-related aspects addressed in existing studies and compares them to our work, as presented in Table 1. The term MEC refers to terrestrial mobile or multi-access edge computing, whereas airMEC pertains to UAV-MEC. In addition, existing studies present three user types. These include general mobile user terminals (gUTs), Internet-of-Things users (IoTs), and vehicular user terminals (vUTs). The various user types indicate distinct movement speeds, including 1.5 m/s for gUTs [16], random vUT speeds ranging from 90 to 120 km/h [15], and classifications of low, medium, and high speeds for mobile IoTs [11]. Nonetheless, the majority of studies addressing gUTs and IoTs within the airMEC context utilize fixed positions, while our study introduces and analyzes the concept of mobility for both airMECs and gUTs.

Moreover, various environments are presented, including highway [12], two-lane road [17], one-lane road [15], generic urban [7,27,28], and ITU-R P.1410 urban [21,22,25]. Our approach distinguishes generic urban environments from those defined by ITU-R P.1410 by employing different line-of-sight (LoS) probability estimation methods for the communication model: generic urban studies use stochastic LoS models, whereas ITU-R studies apply LoS probabilities derived from the ITU urban model [30].

The movement space of mobile nodes is typically characterized using a two-dimensional (2D) Cartesian coordinate system, whereas a three-dimensional (3D) system is discussed in [21,22,25], and [27] within the context of airMEC. Mobility patterns and movement speeds can vary significantly between urban environments. Previous research has predominantly concentrated on basic mobility patterns, including point-to-point movement along straight trajectories [12,17], synchronized random walks [13], and grouped random waypoint navigation at varying velocities [11]. The trajectory-based mobility patterns typically commence with linear or circular configurations, subsequently optimized to reduce offloading latency by reducing distances between users and MEC nodes. Moreover, only a few studies have introduced trace-based mobility patterns, which are more sophisticated, because of their limited generalizability and potential privacy concerns. The Stanford Drone Dataset, which captures pedestrian movements in a university campus environment, is utilized in [16], whereas the user density data from Tencent in Yuelu Mountain is employed in [22]. The mobility patterns of 13,605 taxi cabs in Chengdu City, China, are used in [18].

In addition to implementing and analyzing mobility patterns in many existing studies, mobility impact metrics, such as sojourn time, handover rate, and handover probability, can be utilized to characterize and assess the effects of mobility on wireless networks [31]. Sojourn time indicates the duration a user remains within the coverage area of a serving airMEC before transitioning to another. The handover rate reflects the frequency of these transitions, and the handover probability quantifies the likelihood of a user moving from one node to another. However, a limited number of studies tackle the mobility impact metrics. For example, [16] utilized 2D trace-based mobility data to estimate sojourn time, assuming a user velocity of 1.5 m/s and a distance between the user and the service MEC that is less than the coverage distance. A similar approach is presented in [12,15], and [17], which define the sojourn time as $\mathcal{T}_n = \frac{L}{v_n} - t$, where $\mathcal{T}_n$ represents the sojourn time in time slot n, L denotes the length of the road segment covered by the roadside unit, and v_n indicates the vehicular user's velocity at time slot n. The basic sojourn time models are inadequate for

characterizing the mobility effects of airMEC mobility or ground users in urban environments.

In light of the limitations in mobility impact modeling within urban environments, we extend our research to include mobility-aware fog computing and wireless network studies to validate the presence of these limitations. In the context of computation offloading to fog computing, sojourn time is modeled in [32] as a Gaussian distribution with mean and standard deviation values of $CN(30, 10)$. The Gaussian distribution, while seemingly appropriate, fails to adequately represent the mean and deviation across diverse urban environments. In [33], the sojourn time for a wireless network is modeled as $\sqrt{\frac{2}{3\sqrt{3}}}\frac{1}{v}\sqrt{S_H}$, where v represents the user's velocity and S_H denotes the hexagonal cell size. The research [34] conducted a stochastic geometry analysis of sojourn time in multi-tier cellular networks, revealing an inverse correlation between user velocity and sojourn time, with values of 18.58 s at 0.5 m/s and 2.35 s at 4 m/s. In the context of UAV-assisted wireless networks, the expected sojourn time for a static user at the origin, served by multiple UAVs, has been modeled in [35] for two scenarios. The first scenario involves all UAVs flying at a uniform velocity v, as detailed in (1). The second scenario examines the motion state of UAVs utilizing a probability p_m, as outlined in (2).

$$\mathcal{T}_1 = \frac{4v}{\pi}, \tag{1}$$

$$\mathcal{T}_2 = \frac{1}{2vp_m\sqrt{\lambda}(1-p_m(1-\frac{2}{\pi}))}, \tag{2}$$

where λ is the distribution density of the airborne base stations, which are distributed using the Poisson Point Process (PPP).

Current literature is deficient in studies examining mobility impact metrics on airMEC services, primarily concentrating on optimization solutions during the operational phase, which consider only small or partial task sizes. Table 1 presents a classification of existing studies according to proposed task sizes. The small class is defined as having a task size of 10 Mbits or less, while the large class refers to larger sizes. We selected 10 Mbits due to the capability of commercially available CPUs to compute this quantity within a reasonable timeframe. An Intel Core i9 270H, featuring 14 cores and a maximum turbo frequency of 5.8 GHz, is capable of processing a 10 Mbit task with a medium computation intensity of 500 cycles per bit in under one second.

This paper builds upon the research presented in [31] and investigates the relationship between dynamic urban environments and the mobility of ground users and airMECs concerning computation offloading to airMECs. We developed a game-based mobility simulation within an urban environment to overcome the limitations of basic mobility patterns and the challenges associated with generalizing trace-based mobility methods. A three-dimensional urban environment is implemented using the ITU-R P.1410 urban model. Users' and AirMEC's mobility is generated randomly and managed by artificial intelligence agents to simulate realistic mobility patterns in urban environments, ensuring the avoidance of collisions with buildings. We subsequently utilized the collected data to statistically assess the sojourn time in an urban context. We developed a geometry-based analytical sojourn time to evaluate the validity of our proposed statistical model. A model for offloading task size, contingent upon environmental factors, is proposed, exemplified by scenarios involving omnidirectional and directional antennas.

3. System model

Consider an urban setting equivalent to the depiction in Fig. 1, featuring numerous users traversing the streets alongside multiple airMECs operating overhead to deliver edge computing services. Environmental settings exhibit variability in aspects such as building and street widths, as well as building heights. Furthermore, both users and airMECs are moving at varying speeds and in distinct directions. The airMEC

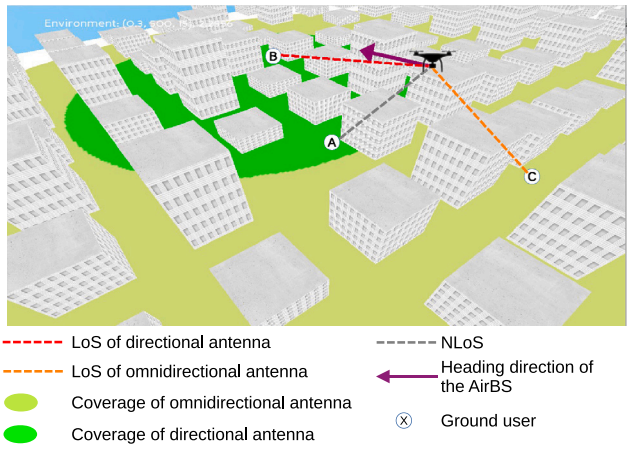

Fig. 1. An illustration of the coverage of an airMEC in an urban setting ($\alpha = 0.3$, $\beta = 500$, $\gamma = 15$). The olive hue indicates the omnidirectional antenna coverage, while the green color shows the coverage of the directional antenna with horizontal and vertical 3-dB beam width equal to 65 degrees. The airMEC traverses the roadway above user B, who possesses a line of sight in both directional and omnidirectional contexts. User A is in the shadow of a building and has an NLoS condition, whereas user C has LoS in the omnidirectional circumstance.

can be equipped with either omnidirectional or directional antennas, which significantly affect the ground coverage patterns and the strength of the communication signal. It is assumed that communication channels utilize high frequencies, such as millimeter waves, to ensure improved communication throughput. Such environments hinder effective communication and increase the likelihood of interruptions, as buildings obstruct signals and diminish coverage for mobile airMECs away from users. As a result, task offloading may either fail or transfer to a different airMEC node, resulting in excessive utilization of inter-airMEC bandwidth and consequently raising time and energy expenditures. This section discusses various components of the realistic system, including the urban environment, airMEC coverage, communication, computation, task offloading, mobility, and sojourn time models. Table 2 presents a list of mathematical symbols.

3.1. Urban environment model

Urban environments are modeled utilizing the parameters α, β, and γ, as defined in ITU-R P.1410 [30], within standard ranges. The α represents the ratio of the built-up area to the total area. The β [buildings/km^2] represents the density of buildings per square kilometer, whereas the γ [meters] denotes the mode of the Rayleigh distribution characterizing building heights. The α ranges from 0.1 for suburban areas to 0.8 for dense urban areas. In a similar manner, the β is defined within the range of 750 to 100, whereas the γ is delineated from 8 m for suburban areas to 50 m for high-rise urban environments.

The density of large stationary obstacles, such as buildings, within a unit area is represented by $\alpha\beta$ [buildings/km^2]. The dimensions of the building and the street are specified in (3) and (4), respectively.

$$w_b = 1000\sqrt{\alpha/\beta}. \tag{3}$$

$$w_s = \frac{1000}{\sqrt{\beta}} - w_b. \tag{4}$$

The urban environment can be modeled using either the PPP distribution or ITU-based variables, as discussed in [36]. Although the PPP lacks the street-grid organization characteristic of modern cities, neither approach provides a method for conducting environmental impact analysis. We propose the simplification of the three parameters of the ITU-R P.1410 model into a single variable as detailed in [37] and

Table 2
List of symbols.

Symbol	Definition	Symbol	Definition
α	The ratio of built-up area to the total area	G_i^o	Omnidirectional antenna's gain of the ith airMEC
β	Number of buildings in a square kilometer	G_j^o	Omnidirectional antenna's gain of the jth gUT
γ	The mode of the Rayleigh distribution of the building heights	$G_i^d(\phi,\theta)$	Directional antenna's gain of the ith airMEC as a function of ϕ and θ
t_s	Length of a time step in discrete simulation	PL	Path loss of signal propagation
w_b	Width of building	$FSPL$	Free space path loss
W_b	Random variable of building's width	A_B	Signal attenuation due to passing through a building
w_s	Width of a street	f_c	Center frequency
$\mathcal{B}$	Channel bandwidth	P_i^{Tx}	Transmit power of the ith airMEC
$\mathcal{E}_c$	Complex representation of urban layout	P_j^{Tx}	Transmit power of the jth gUT
$\mathcal{E}$	Complex argument representation of urban environment in $(-\pi$ and $\pi]$	$P_{i,j}^{Rx}$	Received power from the ith airMEC in the jth gUT
U_a	A set of airMEC	$P_{j,i}^{Rx}$	Received power from the jth gUT in the ith airMEC
U_g	Set of gUTs	$SINR^{o\|d}$	Signal-to-noise plus interference ratio for (omnidirectional | directional)
a_i	The ith airMEC	$\mathbb{E}(\cdot)$	Expectation operator
u_j	The jth gUT	ρ	The reference channel gain
N	Number of airMECs	$\mathbb{A}$	Simulation total area
M	Number of gUTs	S	Set of available services on airMEC
$\theta_{3\text{dB}}$	Vertical 3-dB beamwidth of a directional antenna	s_k	The kth service to be offloaded
$\phi_{3\ \text{dB}}$	Horizontal 3-dB beamwidth of a directional antenna	D_k	Size of the kth task
ϕ	Azimuth angle of the ray connecting airMEC-gUT	q_k	Computation intensity of the kth task
θ	Elevation angle of the ray connecting airMEC-gUT	r_k	Response size of the kth task
C_{a_i}	Center point of the ith airMEC in the ground plane	$T_{G2A}^{o\|d}$	Transmission time of the G2A channel (omnidirectional | directional)
C_{cov}	Center point of coverage ellipse	A_e/P_e	Area and perimeter of coverage ellipse
$\mathbf{v}_{a_i}$	Velocity vector of the ith airMEC	T_i^k	Computation time of the kth task in the ith airMEC
$\mathbf{v}_{u_j}$	Velocity vector of the jth gUT	f_i^k	Computation power allocated in ith airMEC for the kth task
l_{cov}^{θ}	Length of coverage ellipse in the forwarding direction (LCS y-axis)	$T_{A2G}^{o\|d}$	A2G Transmission time to download the result of the kth task in the (omnidirectional | directional)
l_{cov}^{ϕ}	Width of coverage ellipse in the heading direction (LCS x-axis)	$T_{off}^{o\|d}$	Total task offloading time delay in (omnidirectional | directional)
h_i	Altitude of the ith airMEC	$\mathcal{T}^{o\|d}$	Mean sojourn time in (omnidirectional | directional)
$d_{i,j}$	The distance between the ith airMEC and jth gUT	$\boldsymbol{\nu}_{i,j}$	Relative velocity vector between airMEC and gUT
d_o	Horizontal distance between the airMEC and its coverage ellipse	φ	Direction of relative velocity in xy-plane
θ_{dtl}	Down tilt angle of the antenna about the y-axis of the airMEC's LCS	δ	Chord length from velocity–ellipse intersection
θ_{a_i}	Pitch angle of the ith airMEC around the y-axis of its LCS	$C^{o\|d}$	Channel capacity (omnidirectional | directional)
$\bar{\varphi}$	Modular angle of ellipse	$E(m)$	Complete elliptic integral of second kind
$\mathcal{T}_{i,j}$	Pair-specific sojourn time	$D^{o\|d}$	Environment-dependent task size (omnidirectional | directional)
τ_k	Task deadline constraint	$\mathbb{M}$	Mobility control complexity
$\mathbb{L}$	Ray-tracing complexity	$\mathbb{O}$	Optimization algorithm complexity
μ	Von Mises location parameter	κ	Von Mises concentration parameter
$I_0(\kappa)$	Modified Bessel function (order 0)	$\mathcal{T}_{WB}^{o}$	Sojourn time with building and omnidirectional scenario
$\mathcal{T}_{sinr}^{o}$	Sojourn time using SINR and omnidirectional scenario	$\mathcal{T}_{NB}^{d}$	Sojourn time without building and directional scenario
$\mathcal{T}_{WB}^{d}$	Sojourn time with building and directional scenario	$\mathcal{T}_{sinr}^{d}$	Sojourn time using SINR and directional scenario
N_m	Dimension of the navigation mesh		

expressed in (5). Subsequently, broaden the concept to encompass the visualization of urban environments through circular representation, which we will benefit from in later sections.

$$\mathcal{E}_c = (w_s - w_b) + i(w_s - \gamma), \tag{5}$$

where $\mathcal{E}_c$ is the complex representation of an arbitrary urban layout as a function of direct and indirect ITU-R build-up parameters. The expression in (5) is simplified to the complex argument $\mathcal{E}$ [radians], as in (6), to provide a single variable representation of that urban layout.

$$\mathcal{E} = \arg(\mathfrak{T}(\mathcal{E}_c), \mathfrak{R}(\mathcal{E}_c)), \tag{6}$$

where $\mathfrak{R}(\cdot)$ and $\mathfrak{T}(\cdot)$ denote the real and imaginary components of the new representation. $\mathcal{E}$ is uniquely defined within the interval $[-\pi, \pi]$ for any combination of α, β, γ. Table 3 illustrates the complex arguments regarding the standard urban environments chosen by various prior

Table 3
An example of standard urban layouts.

Environment	α	β	γ	$\alpha\beta$	$\mathcal{E}$
Dense urban	0.5	300	20	150	−3.01
High-rise urban	0.5	300	50	150	−2.20
Suburban	0.1	750	8	75	0.90
Urban	0.3	500	15	150	2.26

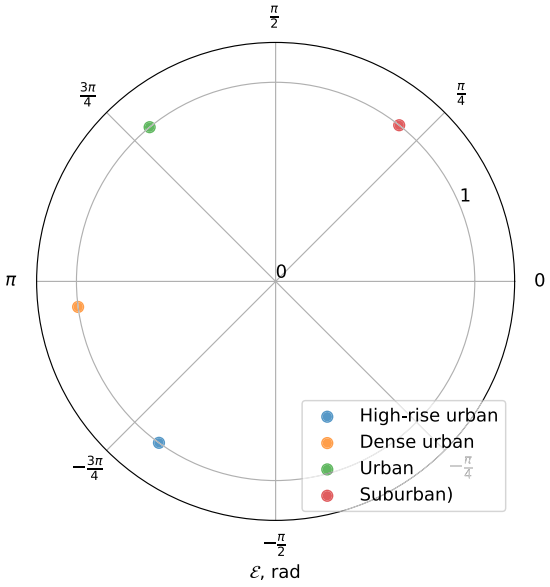

Fig. 2. Polar visualization of the four standard urban layouts using the complex argument as expressed in (6).

studies in the context of LoS probability, including [38,39]. Fig. 2 presents a polar plot illustrating the $\mathcal{E}$ representation of the selected environments.

3.2. Coverage model

Let us consider a set of airMECs denoted by U_a and a set of ground users represented by U_g. Let U_a contain N airMECs, with $a_i \in U_a$ representing an airMEC where $i \in \{0, 1, \ldots, N-1\}$. In a similar manner, $u_j \in U_g$ represents a ground user, where j is an element of the set $\{0, 1, \ldots, M-1\}$. The AirMEC a_i can be outfitted with either an omnidirectional antenna or a directional antenna. This study examines the 3GPP directional antenna as presented in [40]. In a scenario involving an omnidirectional antenna, an airMEC a_i is capable of serving a ground user u_j provided that both can sustain an LoS condition. The urban environment configuration, which includes factors like building density and average building height, influences this condition. The omnidirectional antenna on an airMEC transmits signals in all directions, effectively covering a broad area, except when obstructed by large stationary objects, such as buildings, or by smaller dynamic entities, like another airMEC or a ground user.

The omnidirectional antenna distributes input power uniformly in all directions, leading to an extensive coverage area but reduced signal quality. The use of a directional antenna results in a reduced coverage area but enhances signal strength. The coverage footprint, represented by the ground projection of the directional antenna's main lobe as illustrated in Fig. 3, is influenced by the airMEC altitude, the azimuth beamwidth of the antenna $\phi_{3\ \mathrm{dB}}$ [degree], the zenith beamwidth of the antenna $\theta_{3\ \mathrm{dB}}$ [degree], and the height of the airMEC h_i. A circular coverage projection occurs when both angles are equal. We assume that the azimuth and zenith angles are unequal, leading to an elliptical footprint. The coverage footprint is represented by the light green

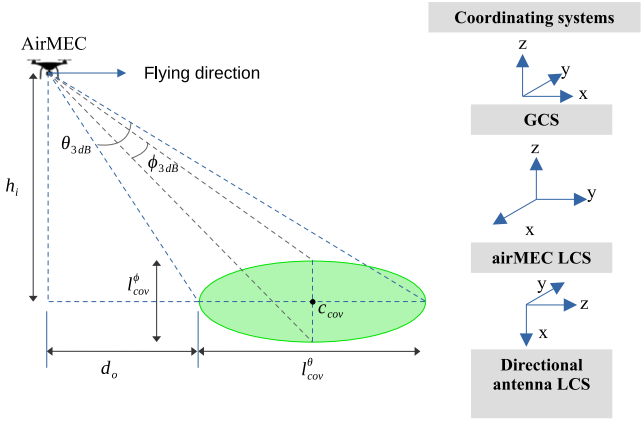

Fig. 3. An example of the directional antenna coverage projection (left side) and an illustration of required transformations from GCS to LCS of the airMEC and the equipped antenna (right side).

ellipse. The dimensions of the ellipse are determined using the three-dB beamwidth angles of the directional antenna. The ellipse's length in the forward (flying) direction of the airMEC is represented by l^{θ}_{cov}, while its width is indicated by l^{ϕ}_{cov}. Estimates are derived from (7) and (8), respectively, with $\theta_{3\ \mathrm{dB}}$ and $\phi_{3\ \mathrm{dB}}$ expressed in radians.

$$l^{\theta}_{cov} = h_i \theta_{3\ \mathrm{dB}}. \tag{7}$$

$$l^{\phi}_{cov} = h_i \phi_{3\ \mathrm{dB}}. \tag{8}$$

It is assumed that the antenna direction is adjustable and can be tilted such that the offset distance d_o represents the horizontal distance from the ground position of the ith airMEC to the nearest end of the coverage projection ellipse. The variable d_o is determined using Eq. (9).

$$d_o = \frac{h_i}{\tan\theta_o}, \tag{9}$$

where θ_o is the offset angle and defined by the equation $\theta_o = 90 - \frac{\theta_{3\ \mathrm{dB}}}{2} - \theta_{dtl} - \theta_{a_i}$. The θ_{dtl} represents the down tilt angle of the antenna relative to the y-axis within the airMEC's local coordinating system (LCS). The θ_{a_i} represents the pitch angle of the ith airMEC about its LCS y-axis.

The center of the coverage projection ellipse is denoted by C_{cov} and calculated in the global coordinating system (GCS) as in (10)

$$C_{cov} = C_{a_i} + \mathbf{v}_{a_i}(d_o + \frac{l^{\theta}_{cov}}{2}), \tag{10}$$

where C_{a_i} is the center point of the ground projection for the ith airMEC location in GCS. $\mathbf{v}_{a_i}$ is the directional velocity vector of the ith airMEC in 3D space. The velocity direction of mobile objects, such as airMECs and ground users, always coincides with the y-axis of their LCS, which is also known as the forwarding direction. Realizing this model, we assume that the directional antenna is mounted on its parent airMEC, where the z-axis of the directional antenna's LCS coincides with the y-axis of the parent airMEC's LCS. The correlation between the antenna's LCS, airMEC's LCS, and GCS is illustrated in Fig. 3.

3.3. Communication model

Ground users are equipped with omnidirectional antennas, while airMECs function under two distinct scenarios: the first employs omnidirectional antennas, and the second utilizes directional antennas. Let the gain of the omnidirectional antenna for the jth ground user be represented as G^o_j, the gain of the omnidirectional antenna for the ith airMEC as G^o_i, and the gain of the directional antenna for the ith airMEC as G^d_i. A significant challenge associated with directional

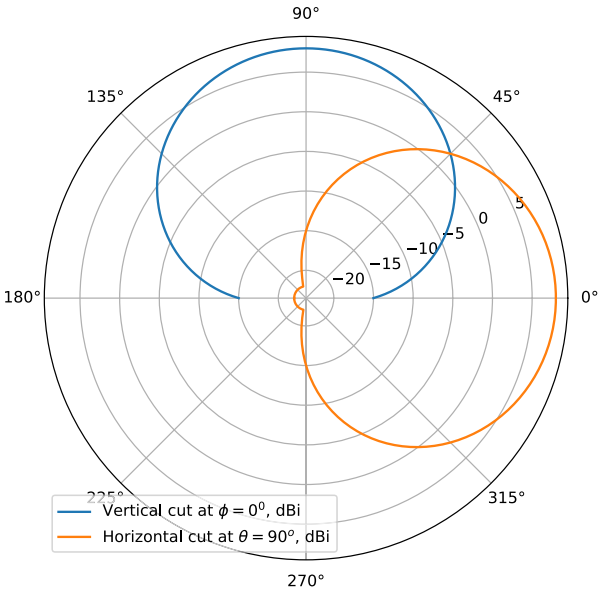

Fig. 4. Radiation pattern of a single element of the 3GPP TR 38.900 antenna.

antennas is the necessity to ascertain the antenna gain in the precise direction of the ground user. The relative transformation of the ground user to the airMEC is established based on the Local Coordinate System (LCS) of the airMEC, followed by the LCS of the antenna. The relative transformation includes the position and Euler angles that convert the GCS into the LCS coordinate system, yielding the elevation angle θ and azimuth angle ϕ, necessary for calculating the directional antenna's gain. The coordinate transformation outlined in Section 7 of 3GPP TR 38.900 is utilized. We utilize the 3GPP directional antenna, as specified in 3GPP TR 38.900, table 7.3–1. The radiation pattern of the 3GPP antenna is illustrated in Fig. 4, with the vertical 3 dB beamwidth $\theta_{3\ \mathrm{dB}}$ and the horizontal 3 dB beamwidth $\phi_{3\ \mathrm{dB}}$ both established at 65°. The maximum radiation power of the 3GPP directional antenna is 8 dBi. Refer to [40] for additional information on GCS, LCS, and 3GPP antennas. The Doppler frequency shift in communication is assumed to be compensable at the receiver.

3.3.1. A2G communication channel

It is assumed that users seek to obtain results by sending tasks to airMECs via the ground-to-air (G2A) communication channel. The airMEC assigned the task will process it and transmit the result back through the air-to-ground A2G channel. We consider asymmetric communication, characterized by unequal data rates between the G2A channel and the A2G channel. To identify the ith airMEC serving the jth ground user, we evaluate the SINR and associate the ground users with their respective airMEC based on the optimal SINR value. We calculate the path loss PL [dB] as shown in (11).

$$PL = \begin{cases} FSPL, \ if \quad LoS \\ FSPL + A_B, \ if \quad NLoS, \end{cases} \tag{11}$$

where $FSPL$ is the free space path loss and is determined by $FSPL = 20\log(d_{i,j}) + 20\log(f_c) - 27.55$, and $d_{i,j}$ is the direct distance in the 3D space. f_c is the center frequency in MHz. A_B is the attenuation of the building, which we set to 40 dB, as suggested in [39].

The $P^{Rx}_{i,j}$ [dB] represents the received power at the jth ground user from the ith airMEC and is determined as

$$P^{Rx}_{i,j} = P^{Tx}_i + G^{o|d}_i - PL + G^o_j, \tag{12}$$

where P^{Tx}_i [dB] is the transmitted power from the ith airMEC. G^o_j [dB] is the omnidirectional antenna gain of the jth user. The antenna gain $G^{o|d}_i$ [dB] depends on the type of antenna that is used. If the airMEC is equipped with an omnidirectional antenna, its gain is denoted as G^o_i [dB]. The gain of the airMEC, when equipped with a directional antenna, is determined by the function $G^d_i = G^d_i(\phi, \theta)$.

The SINR for the jth ground user receiving a signal from the ith airMEC is computed in a manner analogous to the methodology presented in [9].

$$SINR = \frac{P^{Rx}_{i,j}}{\sum I_{/i} + \sigma} \tag{13}$$

where $P^{Rx}_{i,j}$ [dB] is the received power from the ith airMEC in the jth user, $I_{/i}$ is the interference from all airMECs except the ith airMEC, and σ [dB] is the noise. We calculate the $SINR$ for the omnidirectional scenario and the directional scenario, denoting it as $SINR^o$ and $SINR^d$, respectively.

The channel capacity (aka throughput and transmission rate), C^{A2G} [bit per second (bps)], is modeled according to [9] as expressed in (14) and (15) for omnidirectional and directional scenarios, respectively.

$$C^o_{A2G} = \mathcal{B} \cdot \log_2(1 + SINR^o), \tag{14}$$

$$C^d_{A2G} = \mathcal{B} \cdot \log_2(1 + SINR^d), \tag{15}$$

where $\mathcal{B}$ is the bandwidth in [Hertz (Hz)].

3.3.2. G2A communication channel

According to [7], the uplink channel capacity C_{G2A} [bps] can be estimated using the models presented in (16) for omnidirectional antennas, while (17) outlines the throughput for airMECs utilizing 3GPP directional antennas.

$$C^o_{G2A} = \mathcal{B}\log_2(1 + \frac{P^{Tx}_j 10^{(-\rho/10)}}{N}), \tag{16}$$

$$C^d_{G2A} = \mathcal{B}\log_2(1 + \frac{(P^{Tx}_j + G^d_i)10^{(-\rho/10)}}{N}), \tag{17}$$

The transmit power of the ground user is denoted as P^{Tx}_j [W], and ρ represents the reference channel gain. The C^o_{G2A} and C^d_{G2A} represent the G2 A capacity in omnidirectional and directional scenarios, respectively.

3.4. Task offloading model

The ith airMEC is capable of serving multiple services (applications). Each service has the capacity to offload a portion or the entirety of its workload. Let S represent the set of available services in the ith airMEC, and let K denote the total number of services in S. Each service is provided by s_k, where $s_k \in S$ and $k \in \{0, 1, \ldots, K-1\}$. The service s_k is represented by a tuple comprising four elements: the task size D_k [bit], the required computation intensity q_k [cycles/bit] for task processing, the task response size r_k [bit], and the deadline time τ_k [second]. Computation intensity denotes the quantity of CPU cycles necessary to process a single bit of a task. The task is represented by s_k and can be formulated as a tuple, as indicated in (18).

$$s_k = (D_k, q_k, r_k, \tau_k). \tag{18}$$

The paper investigates the influence of urban environments on computational offloading to airMECs. We assess the total offloading time delay for task offloading during three phases: (1) the transmission of the task through the G2 A channel from terrestrial users to airMECs; (2) the computational duration of the task in airMECs to generate the outcome; and (3) the replay of the result back to the owner gUT via the A2G communication channel. The Eqs. (16) and (17) specify the G2 A transmission duration for the kth task, characterized by a data size of D_k. This concept is further illustrated in (19) and (20) for omnidirectional and directional contexts, respectively.

$$T^o_{G2A} = \frac{D_k}{C^o_{G2A}}, \tag{19}$$

$$T^{d}_{G2A} = \frac{D_k}{C^{d}_{G2A}}. \tag{20}$$

When the ith airMEC serves the kth task from the jth ground user, the estimated time of task computation is denoted by T^{k}_{i} [second] and is expressed in (21)

$$T^{k}_{i} = D_k \frac{q_k}{f^{k}_{i}}, \tag{21}$$

where f^{k}_{i} [cycle/second (Hz)] is the allocated computation power (CPU cycles) in the ith airMEC for the kth service task.

Based on (14) and (15), (22) and (23) express the A2G transmission time required to download the result of task computation for omnidirectional and directional scenarios, respectively.

$$T^{o}_{A2G} = \frac{r_k}{C^{o}_{A2G}}. \tag{22}$$

$$T^{d}_{A2G} = \frac{r_k}{C^{o}_{A2G}}. \tag{23}$$

The total task offloading time delay is denoted by T^{o}_{off} as expressed in (24) and T^{d}_{off} as expressed in (25) for omnidirectional and directional scenarios, respectively.

$$T^{o}_{off} = T^{o}_{G2A} + T^{k}_{i} + T^{o}_{A2G}, \tag{24}$$

$$T^{d}_{off} = T^{d}_{G2A} + T^{k}_{i} + T^{A2G}_{o|d}. \tag{25}$$

3.5. Mobility model

In contrast to the simple synthetic mobility models found in existing literature, we propose an urban-aware mobility, which is defined as follows: Buildings serve as enduring impediments within three-dimensional space. User and airMEC movements are permitted in open spaces that represent street areas or at a height of five meters above the average of the Rayleigh distribution of building heights. Mobile objects can navigate in three-dimensional space while avoiding collisions with buildings and other smaller mobile entities. We regulate the velocity and apply physics principles to control the acceleration and deceleration of mobile objects. We implement stop points between movements, where mobile objects remain stationary for brief intervals, to model human mobility patterns in trace-based mobility types.

To realize this urban mobility pattern, a 3D mobility simulation has been developed in [37], which incorporates AI-based mobility agents for the movement of game objects. We develop a mobility manager that obtains mobility points from the navigation mesh file, assigns mobility targets to users and airMECs, and monitors the status of mobile objects. An AI mobility agent is assigned to each user and airMEC. The agent communicates the mobility status to the manager at each time interval. In the case of a static mobile node, the manager designates a mobility target for it. Upon receiving the new target, the agent computes the shortest path from its current location to the mobility target by employing the A-star algorithm, which leverages the navigation mesh of the evaluated urban environment. Upon arrival at its destination, the mobile node remains until it acquires a new target.

We develop a navigation mesh for each urban configuration to enable the autonomous navigation of mobile entities, considering the dimensions of buildings and roadways. A street map is generated for each urban setting using (3) and (4). The map is stored in the repository for subsequent identical mobility simulations. We also use it to assign navigation mesh nodes to street polygons. The step size of the navigation mesh grid is created by rounding the $\frac{\sqrt{\mathbb{A}}}{w_b + w_s}$. The mobility manager identifies the nodes within the mesh and randomly allocates new mobility targets to users and airMECs. To simplify the generation of navigation meshes, we utilize computer vision techniques to identify street pixels, typically represented in black, and subsequently append their coordinates to the mobility manager following orientation conversion.

3.6. Sojourn time

The sojourn time, also referred to as service time, represents the expected duration a user remains within the coverage area of a serving airMEC. This metric is crucial for assessing the impact of mobility on wireless networks. This study presents two methodologies for estimating sojourn time in urban settings. The first approach is statistical and applicable to both omnidirectional and directional antenna scenarios within any ITU-based urban environment. The second is analytical and is designed to assess the accuracy of the statistical method. The analysis is applicable solely to generic environments when employing directional antennas.

3.6.1. Statistical sojourn time

We assume that ground users communicate with airMECs using millimeter-wave frequencies to enable high data rates. High frequencies require the maintenance of LoS conditions to establish the communication channel. This property is utilized to ascertain the sojourn time, wherein users can access the service only when they maintain a clear line of sight with the serving airMECs. It is assumed that the first Fresnel zone is negligible and can be disregarded in the absence of an optical line of sight. To collect the ray-tracing LoS conditions between mobile users and airMECs, we created a game-based simulation that implements a 3D synthetic urban environment. We employ advanced geometry-based features of game engines, including transformation calculations and collision detection, to gather the ray-tracing status. The ray-tracing technique facilitates the collection of precise data and is employed in LoS probability modeling, as demonstrated in the study [31,38].

Urban configurations are presumed to adhere to the ITU-R P.1410 model. Ray-tracing LoS data is collected for both omnidirectional and directional antenna scenarios. The implementation of omnidirectional antennas on airMECs facilitates positive LoS conditions for users over extended distances along the same street. Thus, we establish the relationship between users and airMECs through the SINR to assess a specific connected sojourn time in ITU-based environments. The omnidirectional scenario in generic environments is overlooked, as neither mobility patterns nor speed lead to communication loss due to the continuous presence of positive LoS throughout the experiment. The limited coverage of airMECs in the directional antenna scenario results in frequent non-line-of-sight conditions and communication losses.

Upon collecting the ray-tracing LoS data, we estimate the sojourn time by scoring the consecutive time slots that indicate positive LoS for each pair of gUTs and airMECs. The averages of all urban environments are subsequently fitted using a cubic polynomial method. We developed a geometry-based mathematical model to assess the influence of directional antenna scenarios and urban mobility on sojourn time in various environments, ensuring the accuracy and applicability of the statistical approach. The generic environments are identical to the ITU-based environment, utilizing the same street maps and random seeds for generating mobility patterns. The sole distinction lies in the removal of buildings from the generic scenario. Validating the sojourn time in a directional antenna scenario is sufficient, as the directional line of sight constitutes a subset of the omnidirectional LoS.

3.6.2. Analytical sojourn time

In contrast to the models (1) and (2) presented in [35], we propose a geometry-based mathematical model for sojourn time that accounts for active mobile users and airMECs. Fig. 5 depicts the modeled environment, considering mobility directions, velocities, and environmental settings, which are key to preserving LoS conditions. Consequently, we ascertain the sojourn time. In time slot t_0, the coverage of the ith airMEC extends to ground users u_1, u_2, and u_3, each moving at varying velocities and in different directions. The duration of service for each user of airMEC will vary. The duration is contingent upon the magnitude and direction of the user's relative speed to the airMEC. The

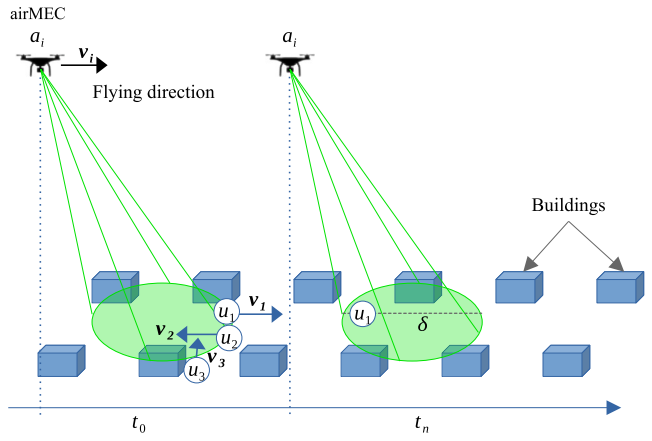

Fig. 5. An example of the impact of mobility direction, velocity, and urban environment on the sojourn time is in the case of using a directional antenna.

lengths of the velocity vectors for each user in the figure indicate their respective speeds and directions. Consequently, they will encounter varying distances while traversing the coverage ellipse. Their sojourn times will consequently vary. For instance, the service will be lost in the order u_3, u_2, u_1, unless a building obstructs the maintained line-of-sight condition prior to the exit of these users from the coverage ellipse in time slot t_n.

To characterize a reliable sojourn time with environment-dependent mobility, we minimize the dynamic velocities observed during the acceleration and deceleration of mobile objects, as well as the stationary periods, to approximately one time slot. The duration of the jth user within the coverage area of the ith airMEC is determined by calculating the relative speed in the GCS domain. The forward orientation of a mobile object consistently aligns with the y-axis of its LCS, as illustrated in Fig. 3. The mean velocities of the ith airMEC and the jth gUT are denoted as $\boldsymbol{v}_i$ and $\boldsymbol{v}_j$, respectively. The relative velocity is represented by $\boldsymbol{v}_{i,j}$ and is articulated in (26).

$$\boldsymbol{v}_{i,j} = \boldsymbol{v}_i - \boldsymbol{v}_j. \tag{26}$$

Let φ [radian] represent the direction of the relative velocity within the xy plane. The expected relative velocity is represented in (27).

$$|\boldsymbol{v}_{i,j}| = \sqrt{v_i^2 + v_j^2 - 2v_i v_j \cos\varphi}. \tag{27}$$

The length of the chord resulting from the intersection of relative velocity and the elliptical coverage projection is denoted by δ [meter]. In case this chord passes through the ellipse center, it can be determined using (28). However, the random nature of mobility patterns does not guarantee a relative velocity dose. Consequently, we employ a more sophisticated and general approach grounded in the Crofton formula, which estimates the expected length of the chord for a convex body as expressed in (29), where A_e and P_e are the area and the perimeter of the coverage ellipse.

$$\delta = \frac{2\left(\frac{l^{\theta}_{cov}}{2}\right)\left(\frac{l^{\phi}_{cov}}{2}\right)}{\sqrt{\left(\frac{l^{\theta}_{cov}}{2}\right)^2 \sin^2(\varphi) + \left(\frac{l^{\phi}_{cov}}{2}\right)^2 \cos^2(\varphi)}}. \tag{28}$$

$$\mathbb{E}(\delta) = \frac{\pi A_e}{P_e}. \tag{29}$$

The area of the coverage ellipse is expressed in (30).

$$A_e = \frac{\pi}{4} l^{\theta}_{cov} l^{\phi}_{cov}. \tag{30}$$

The perimeter of the coverage ellipse P_e can be approximated as (31)

$$P_e \approx \pi\left[3\left(\frac{l^{\theta}_{cov}}{2} + \frac{l^{\phi}_{cov}}{2}\right) - \sqrt{\left(3\frac{l^{\theta}_{cov}}{2} + \frac{l^{\phi}_{cov}}{2}\right)\left(\frac{l^{\theta}_{cov}}{2} + 3\frac{l^{\phi}_{cov}}{2}\right)}\right], \tag{31}$$

Based on [41], the exact perimeter of the ellipse can be numerically estimated using the complete elliptic integral of the second kind $E(m)$ as expressed in (32)

$$E(m) = \int_0^{\pi/2} \sqrt{1 - m\sin^2(t)}\, dt, \tag{32}$$

where $m = \sin^2(\bar{\varphi})$ is the parameter of the elliptic integral and $\bar{\varphi} = \cos^{-1}\left(\frac{l^{\phi}_{cov}}{l^{\theta}_{cov}}\right)$ is the modular angle of the ellipse. Then the exact perimeter of the coverage ellipse is determined in (33), where $E(m)$ can be numerically calculated using mathematical tools, such as *scipy.special.ellipe*.

$$P_e = 4\frac{l^{\theta}_{cov}}{2} E(m) = 2l^{\theta}_{cov} E(m). \tag{33}$$

Then, we determine the expected length of δ by substituting (30) and (33) in (29)

$$\mathbb{E}(\delta) = \frac{\pi^2 l^{\phi}_{cov}}{8E(m)} \tag{34}$$

Finally, the expected sojourn time $\mathcal{T}_{i,j}$ of the jth user in the coverage of the ith serving airMEC is determined in (35).

$$\mathcal{T}_{i,j} = \frac{\mathbb{E}(\delta)}{|\boldsymbol{v}_{i,j}|}. \tag{35}$$

4. Core methodology

This section presents the main methodology employed to fulfill the study's objective, alongside the specific methods detailed in the system model. Due to the scarcity of available datasets characterizing mobility in urban settings, we have created a 3D environment-aware mobility simulation framework called Panda5gSim [37]. The Panda5gSim is utilized to generate numerous urban environments and simulate user and airMEC mobility for the collection of trace-based data. The trajectories for users and airMECs are calculated by identifying the shortest path using the A-star algorithm, which is integrated into the PandaAI engine.

Urban environments are synthetically generated utilizing the ITU-R P.1410 parameters (α, β, and γ) and considerations outlined in Section 3.1. Standard ranges for these parameters are established, with α defined between 0.1 and 0.7, β ranging from 100 to 750 buildings per square kilometer, and γ specified from 8 to 50 m. To establish a uniformly distributed urban environment within the range $-\pi \leq \mathcal{E} \leq \pi$, we employ the Poisson Point Process (PPP) to generate 1000 points for each parameter, adhering to the lower and upper limits set by the ITU-R guidelines. The thinning property of PPP is utilized to select an environment at every 5-degree interval of the circular representation of the complex argument $\mathcal{E}$. The dimensions of buildings and streets are calculated through Eqs. (3) and (4). Randomized placements of streets and buildings are generated for each urban environment to create a two-dimensional map of the respective urban setting. The maps generated from the initial simulation run are preserved for the creation of navigation meshes for mobility and for subsequent iterations necessary to validate the rigor and integrity of the results.

The simulation of mobility is achieved through the implementation of game actors representing users, as well as airMECs modeled as humanoids and quadcopters. The initial positions of users and airMECs are randomly chosen from navigation nodes situated within road polygons. The mobile devices (gUTs) are affixed to the right hands of the humanoids, which move as the humanoids walk or run. The variation in the heights of the gUTs ranges from 1 to 1.5 m. A mobility manager

is introduced to regulate the movement of users and airMECs. The coordinates of the street navigation grid nodes are employed to create the pool of mobility targets. The mobility manager evaluates the status of mobility agents for mobile actors and designates their mobility destinations, as outlined in Section 3.5. The altitudes of airMECs are fixed at 100 m to assess the analytical and statistical sojourn time, facilitating the validation of statistical precision.

Trace-based data is gathered at each time slot throughout the mobility simulation. The data collected for each user–airMEC pair comprises the following elements: The urban setting name, ray-tracing LoS conditions for omnidirectional and directional antennas, transformation tuple, directional antenna gain, free-space path loss, altitude difference, three-dimensional and two-dimensional distances, velocities of the user and airMEC, and the number of buildings between each node pair. The ray-tracing LoS refers to the optical line of sight, established through game-based ray collision detection methods. The quantity of buildings situated between the user and airMEC is gathered for validation against LoS data. The transformation tuple comprises five components: the user's transformation in GCS, the airMEC's transformation in GCS, the relative transformation of the user to the LCS of the airMEC, the user's ID, and the airMEC's ID. A node's transformation encompasses its position in three-dimensional space and its orientation relative to a reference coordinate system, quantified using Euler's transformation angles expressed in degrees. The gain of the directional antenna is established according to the model presented in Section 3.3.

The simulation is performed for three iterations in the initial round. Each urban setting is allocated 120 s. The duration of a single simulation run is 8640 s. Data is collected from three simulation runs, each involving 72 environmental settings, which included buildings. The heights of buildings are generated randomly using the Rayleigh distribution to maintain the generality and randomness of the experiments, as outlined in Section 3.1. The initial locations of mobile actors and mobility targets are selected randomly from the nodes of the navigation grid. Consequently, varying building heights and mobility will be produced. A subsequent simulation round with three runs is conducted in the same urban settings, excluding buildings, to assess their impact. The mobility patterns remain consistent with those observed in the initial round, utilizing identical random seeds. The data gathered in the second round of generic environments devoid of buildings serves to validate the statistical model's accuracy in comparison to the analytical model. This method overcomes the limitations of geometry-based analytical approaches in modeling dynamic urban environments, which depend on specific assumptions associated with geometry-based models. Our approach demonstrates that the proposed statistical model is accurate in the context of directional antennas, which is critical for urban communication.

We examine data validation from various perspectives throughout the experiments. Initially, we gather transformations, two-dimensional ground distances, and three-dimensional distances to manually verify the game-based measurements using randomly selected records. The quantity of buildings produced from the ray collision detection involving user–airMEC pairs is utilized to verify the precision of the ray-tracing LoS conditions. The statistical sojourn time approach described in Section 3.6.1 is validated against the mathematical model presented in Section 3.6.2 for constant and dynamic velocities. The constants represent the mean velocities assigned to airMECs and users, whereas the dynamics arise from the acceleration and deceleration of speeds at the beginning of movements or upon the arrival of objects at their destinations. Additionally, we present an SINR-based method for associating users with their serving airMECs. We estimate the sojourn time for each user–airMEC pair based on SINR, applying a 40 dB signal loss for each building recorded in the collected data. The SINR-based method, while not our preferred approach due to its complete dependence on stochastic communication models in generic environments, offers a stochastic evaluation that validates the plausibility of our models. Because this study represents the first attempt to assess the combined effects of mobility and urban environment, further analysis is conducted to elucidate various aspects and correlations, including the influence of building and street dimensions, handover occurrences, and the Von Mises directionality analysis.

5. Complexity analysis

The measurement of urban mobility impact is often contingent upon the availability of trace-based mobility data, necessitating substantial financial resources, personnel, and extended periods for collection. The proposed approach utilizes a game-based simulation to gather trace-based mobility and ray-tracing line-of-sight data across numerous urban environments within a matter of hours. Furthermore, we examine the computational complexity of the proposed method through the utilization of three independent factors. The initial factor is the complexity involved in generating synthetic urban environments and navigation meshes, which is contingent upon the building density $\alpha\beta$ and the dimensions of the navigation mesh (N_m). The complexity is estimated as $\mathcal{O}(8N_m^2 + \alpha\beta)$ for the first simulation run, with each navigation node having 8 potential edges to neighboring nodes. The complexity in consecutive runs is constrained to $\mathcal{O}(\max(\mathbb{M}, \mathbb{L}))$, with $\mathbb{M}$ representing the complexity associated with controlling mobility patterns and trajectories, estimated as $\mathbb{M} = \mathcal{O}(N + M)$. The complexity of gathering ray-tracing LoS, denoted as $\mathbb{L}$, is defined by the equation $\mathbb{L} = \mathcal{O}(N \cdot M \cdot \alpha\beta)$, representing the third factor in the analysis.

Nonetheless, the complexity of this approach is minimal in comparison to trace-based mobility collections and the possible decrease in computational complexity achieved through the application of sojourn time models in optimization methods. Let the complexity of a specific optimization algorithm be denoted by $\mathbb{O}$. The overall complexity can be evaluated for independent, dependent, and nested combinations of $\mathbb{M}$, $\mathbb{L}$, and $\mathbb{O}$, yielding $\mathcal{O}(\max(\mathbb{M}, \mathbb{L}, \mathbb{O}))$, $\mathcal{O}(\mathbb{M} + \mathbb{L} + \mathbb{O})$, and $\mathcal{O}(\mathbb{M} \cdot \mathbb{L} \cdot \mathbb{O})$ computational complexities, respectively. The incorporation of the sojourn time model into optimization methods, rather than relying on mobility patterns or trajectory control, can simplify the complexity of $\mathbb{M}$ and $\mathbb{L}$ to a single constraint [15], which can be executed within a comparison instruction. Current research examining sojourn time, as indicated in Table 1, overlooks the probability of LoS, as the consideration of sojourn time presupposes the presence of an optical line of sight. Consequently, we assert that the models presented in Section 6 will substantially decrease the overall complexity of future optimization methods to $\mathcal{O}(\mathbb{O})$.

6. Results and discussions

6.1. Experimental setup

Two experimental scenarios[1] simulate a total of 72 urban settings. The first includes buildings to statistically quantify the sojourn time. The second excludes buildings and preserves street configurations and mobility patterns to assess the accuracy of the statistical against the analytical sojourn times, as well as measuring the effect of buildings on the statistical models. The circular distribution of the generated urban environments is presented in 6. We utilize ten users and two airMECs, maintaining active mobility at average velocities of 3 [m/s] and 30 [m/s], respectively. We compute the radio link budget for the A2G communication channel at a central frequency of 28 GHz. The transmit power of the airMEC is configured to 43 [dB], and the gain of the omnidirectional antenna is set to 1 [dB]. The directional antenna gain is calculated according to its radiation pattern. The signal experiences an attenuation of 40 dB while traversing the building. The remaining simulation parameters are described in Table 4.

[1] Video examples using point actors where red points are airMECs and blue points are ground users: (1) Dense Urban without buildings; (2) Dense Urban with buildings. Camera position (0, −900, 150), the horizontal field of view of the camera lens is 70 degrees and the aspect ratio is 30 degrees.

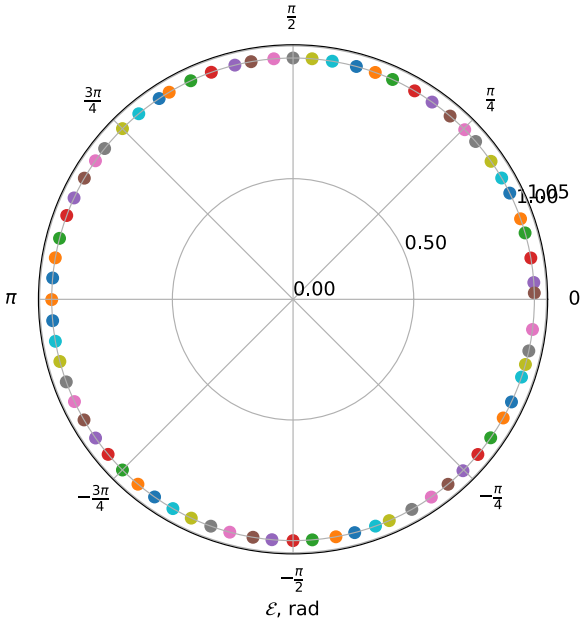

Fig. 6. A polar plot showing the distribution of 72 urban environments within the range of $\mathcal{E}$. A list of parameter values is presented in Appendix A.

The collected ray-tracing data for omnidirectional and directional antenna scenarios is gathered concurrently for each time slot, and mobility is simulated for 120 s for each environment. The mean of three independent runs for the 72 environments is reported and formulated in the final statistical models. The trace-based data is collected using Panda5gSim [37], an open-source tool accessible at https://github.com/yemenlinux/panda5gsim. We perform analysis and data visualization utilizing NumPy, SciPy, and several other Python modules. We use the Ubuntu Linux operating system on a Dell Precision 7530 equipped with a 12-core i9-8950HK CPU working at 2.90 GHz and 32 GB of RAM. The subscript NB denotes generic urban areas, whereas the subscript WB refers to ITU-based urban areas that include buildings. The subscript $sinr$ is utilized to ascertain the service time within the stochastic communication model for associating user–airMEC pairs. The superscripts d and o denote directional and omnidirectional antennas, respectively.

6.2. Data validation

The trace-based data comprises six files, each corresponding to a distinct simulation run. Three files pertain to the initial experimental scenario involving buildings, whereas the other three files relate to the subsequent experiment that does not include constructions. Each file contains 16 columns and 174,240 records, with each urban setting represented by 2240 records. Each experiment comprises 7260 records per environment, resulting in a cumulative total of 522,720 records. The cumulative total of records across both experiments is 1,045,440. The data collected is detailed and presented in [42].

Fig. 7 illustrates the deviation of the proposed statistical approach from the analytical method in the context of directional antennas utilized within generic urban environments. A horizontal line at 6.225 s indicates the analytical sojourn time for constant speeds of 3 m/s for users and 30 m/s for airMECs. The original ray-tracing sojourn time is estimated by counting line-of-sight conditions, revealing higher values than the mean analytical value within the range $[-\pi, 0]$. This range corresponds to dense, high-rise urban environments, where narrower street

Table 4
Default values of simulation parameters.

Parameter	Meaning	Value
$\mathbb{A}$	Simulation total area	(1200 × 1200) m^2
T_{sim}	Total simulation time	120 s/environment
M	Number of gUTs	10
N	Number of airMECs	2
h_j	Height of the jth gUT	Random (1, 1.5) m
h_i	Height of the ith airMEC	$U(50, 1000)$ m
$\mathbf{v}_{u_j}$	Mean velocity of the jth gUT	3 m/s
$\mathbf{v}_{a_i}$	Mean velocity of the ith airMEC	30 m/s
f_c	Center frequency	28 GHz
$\mathcal{B}$	Channel bandwidth	10 MHz
f_{MEC}	MEC Computation power	25 GHz
D_k	Offloading task size	$CN(5, 500)$ Mbits
q_k	Task computation intensity	1000 cycles/bit
r_k	Task's result size	$0.25D_k$ Mbits
P_j^{Tx}	Users' transmission power	0.5 W
P_i^{Tx}	AirMECs' transmission power	20 W
$\theta_{3\ \mathrm{dB}}$	Vertical 3 dB beamwidth of a directional antenna	65°
$\phi_{3\ \mathrm{dB}}$	Horizontal 3 dB beamwidth of a directional antenna	65°

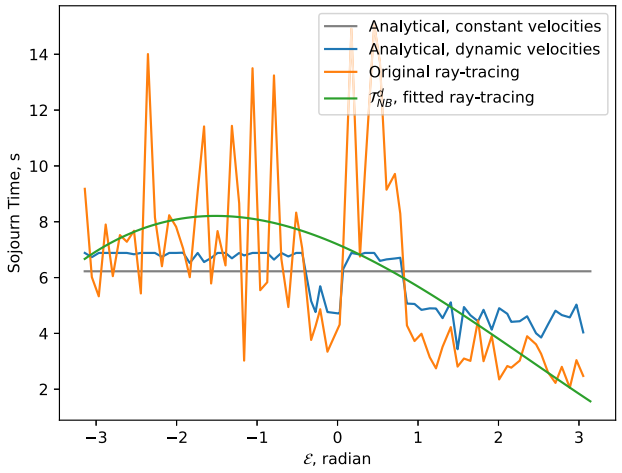

Fig. 7. The variation between the proposed statistical and analytical models is based upon the environment when cities are simulated devoid of buildings.

widths necessitate deceleration of mobile objects at intersections. In the interval from $\frac{\pi}{2}$ to π within urban environments, the increased availability of open roads facilitates higher acceleration, resulting in reduced sojourn times. This justification can be confirmed through analyzing the dynamic velocities resulting from the acceleration and deceleration of mobile objects. The sojourn time of the analytical model for velocities differing from the mean exhibits a similar trend to the original across all environmental ranges, with the exception of the suburban area. In the interval from 0 to $\frac{\pi}{2}$, which represents suburban regions, the street polygons exhibit greater width owing to the relatively small built-up area relative to the total area. This situation facilitates an increase in navigation nodes, permitting the A-star algorithm to choose trajectories that necessitate directional changes and, as a result, deceleration. To address the erratic characteristics of the original sojourn time, we employ a cubic polynomial approximation. The resulting model $\mathcal{T}^d_{NB}$ shows a deviation of 0.37 percent from the analytical model under constant velocities and 3.81 percent under dynamic velocities due to acceleration and deceleration. The constant speeds, which are within a margin of ±5 percent of the average speeds listed in Table 4, account for approximately 3.7 percent of the total data. Thus, the overall deviation is 1.84 percent.

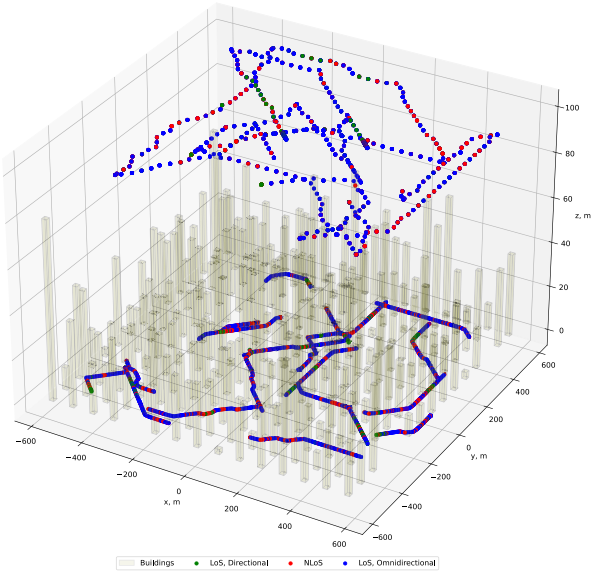

Fig. 8. Example of mobility patterns for two airMECs and 10 gUTs in an environment setting ($\alpha = 0.19, \beta = 149, \gamma = 23$). These patterns represent two simulation runs lasting 120 s each.

6.3. Mobility patterns

Fig. 8 illustrates the mobility patterns for users and airMECs within the urban configuration characterized by parameters ($\alpha = 0.19, \beta = 149, \gamma = 23$). The colors of the scattered spots represent the LoS conditions between each user–airMEC pair: red indicates a non-line of sight (NLoS), blue signifies LoS in an omnidirectional antenna scenario, and green reflects the existence of LoS in a directional antenna scenario. The mobility patterns are aligned with the street configuration, thereby preventing collisions with buildings. The distance between points reflects the velocities of the mobile objects, where shorter distances are associated with lower speeds and longer distances are associated with higher speeds. The walking paths of ground users display high density and overlap spots as a result of their lower speed. The trajectories of airMECs exhibit longer distances between points, except where airMECs change direction because they decelerate.

6.4. Building effect on sojourn time analysis

Fig. 9 compares the sojourn time when using omnidirectional antennas in ITU-based urban settings that include buildings ($\mathcal{T}^o_{WB}$) to the SINR-based user–airMEC pairs association ($\mathcal{T}^o_{sinr}$). The mean sojourn times are 16.67 and 12 s for $\mathcal{T}^o_{WB}$ and $\mathcal{T}^o_{sinr}$, respectively.

Fig. 10 shows the sojourn time of the directional antenna scenario. The $\mathcal{T}^d_{NB}$ represents the sojourn time where buildings are not generated. Experiments with buildings are shown in the $\mathcal{T}^d_{NB}$, while the $\mathcal{T}^d_{sinr}$ shows the measured sojourn time by connecting to the best SINR. The mean sojourn times for $\mathcal{T}^d_{NB}$, $\mathcal{T}^d_{WB}$, and $\mathcal{T}^d_{sinr}$ are 6.15 s, 5.93 s, and 6.26 s, respectively.

We present our findings in Figs. 9 and 10 through a closed-form mathematical expression. The proposed statistical environment-dependent sojourn times are formulated as cubic polynomials, as expressed in (36) with the parameters a_i detailed in Table 5.

$$\mathcal{T}(\mathcal{E}) = \sum_{i=0}^{3} a_i \mathcal{E}^{3-i}, \tag{36}$$

The environment-dependent expected sojourn time, as modeled in (36), can be directly utilized, or the sojourn time can be stochastically distributed using the Gaussian distribution with the mean and variance

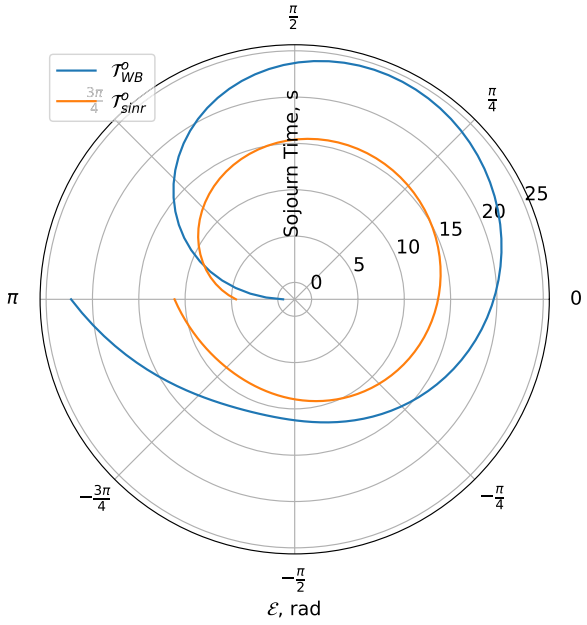

Fig. 9. The mean sojourn time in the omnidirectional scenario along the environment complex argument $\mathcal{E}$, where $\mathcal{T}^o_{WB}$ is measured by ray-tracing and $\mathcal{T}^o_{sinr}$ is measured by connecting the ground user to the airMEC with the best SINR.

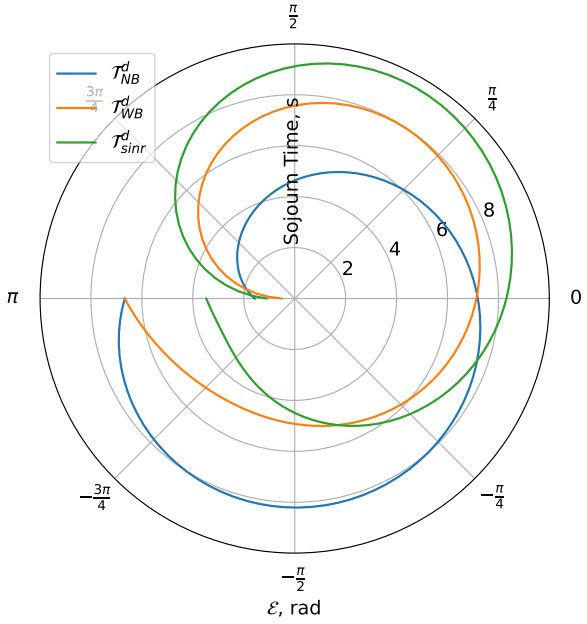

Fig. 10. The mean sojourn time in the directional scenario along the environment complex argument $\mathcal{E}$, for no buildings $\mathcal{T}^d_{NB}$, with buildings $\mathcal{T}^d_{WB}$, and by connecting to the best SINR $\mathcal{T}^d_{sinr}$.

specified in Table 5. The stochastic nature of SINR-based models limits their ability to quantify the impact of urban environments; therefore, their use in characterizing these environments is not recommended. If necessary, it is feasible to utilize the variance of the models $\mathcal{T}^o_{WB}$ and $\mathcal{T}^d_{WB}$ within the Gaussian distribution of the models $\mathcal{T}^o_{sinr}$ and $\mathcal{T}^d_{sinr}$, respectively.

Analysis of the impact of buildings on sojourn times reveals an average difference of approximately 0.34 s between $\mathcal{T}^d_{WB}$ and $\mathcal{T}^d_{sinr}$, and

Table 5
Fitting parameters of the proposed statistical sojourn times.

Sojourn time	a_i 0	1	2	3	Mean (s)	Variance (s)
$\mathcal{T}^o_{WB}$	−1.03	−0.89	6.50	19.66	16.67	9.03
$\mathcal{T}^o_{sinr}$	−0.42	−0.59	3.09	13.65	11.67	–
$\mathcal{T}^d_{NB}$	0.04	−0.31	−1.24	7.19	6.15	3.36
$\mathcal{T}^d_{WB}$	−0.25	−0.36	1.45	7.13	5.93	2.52
$\mathcal{T}^d_{sinr}$	−0.25	−0.61	2.09	8.31	6.26	–

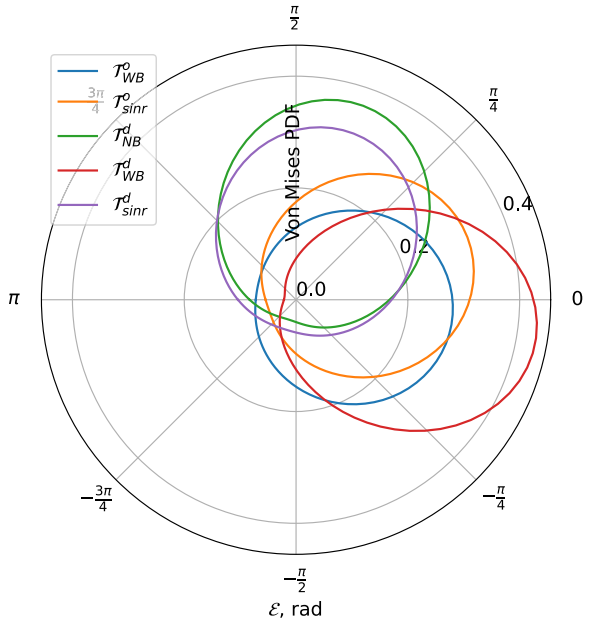

Fig. 11. The Von Mises PDF of sojourn time distribution.

Table 6
The fitting parameters of the Von Mises distribution.

Parameter	$\mathcal{T}^o_{WB}$	$\mathcal{T}^o_{sinr}$	$\mathcal{T}^d_{NB}$	$\mathcal{T}^d_{WB}$	$\mathcal{T}^d_{sinr}$
μ	−0.13	0.33	1.26	−0.18	1.27
κ	0.68	0.92	1.14	1.51	0.86

about 0.22 s between $\mathcal{T}^d_{NB}$ and $\mathcal{T}^d_{WB}$, equating to roughly 3.77 percent. The directions of peak values for the statistical models differ among them. We analyze the circular direction distribution of the ray-tracing sojourn times utilizing the Von Mises distribution, characterized by the probability distribution function (PDF) presented in (37).

$$f(\mathcal{E}|\mu,\kappa) = \frac{\exp(\kappa\cos(\mathcal{E}-\mu))}{2\pi I_0(\kappa)}, \tag{37}$$

where μ is the distribution location, κ is the concentration of the distribution, and $I_0(\kappa)$ is the modified Bessel function of the first kind of order 0.

Fig. 11 illustrates the Von Mises probability density function (PDF) for both omnidirectional and directional sojourn times in settings devoid of and containing buildings. We apply the Von Mises distribution to fit the second polynomial statistical sojourn time. The Von Mises fitting parameters are displayed in Table 6. The omnidirectional examples exhibit lower concentration in the distribution direction compared to the directional ones. The $\mathcal{T}^d_{NB}$ is oriented towards the suburban area when $w_s > w_b$ and $w_s > \gamma$. The experimental results concerning buildings indicate that the peak orientations of $\mathcal{T}^o_{WB}$ and $\mathcal{T}^d_{WB}$ are directed towards $\mathcal{E} \approx 0$, where $w_s > w_b$ and $w_s \approx \gamma$.

By comparing the distribution orientations of $\mathcal{T}^o_{WB}$ and $\mathcal{T}^d_{WB}$ with $\mathcal{T}^o_{sinr}$ and $\mathcal{T}^d_{sinr}$ in Fig. 11, it is evident that the computation of sojourn time utilizing SINR-based metrics has resulted in an anti-clockwise rotation of the probability direction towards the suburban area, losing the alignment between directional and omnidirectional scenarios. Nonetheless, employing SINR-based metrics is a specific instance we have presented to facilitate the calculation of communication channel capacities for characterizing the offloading task size, which will be elaborated upon subsequently. The parameters introduced for $\mathcal{T}^o_{WB}$, $\mathcal{T}^d_{NB}$, and $\mathcal{T}^d_{WB}$ in Table 5 are generalizable and applicable to different connection-based methodologies, including distance, received power, or linking a user to several airMECs.

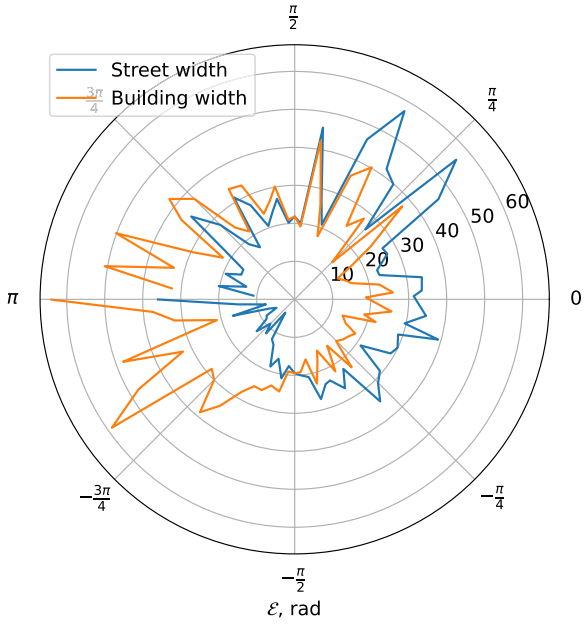

Fig. 12. The street and building width distribution for the 72 urban environments used.

Table 7
Fitting parameters of capacity.

Channel capacity	a_i 0	1	2	3	Mean
$C^o_{G2A}(\mathcal{E})$	0.07	0.01	−0.78	180.48	180.51
$C^d_{G2A}(\mathcal{E})$	0.07	−0.01	−0.99	222.85	222.82
$C^o_{A2G}(\mathcal{E})$	4.56	4.51	−43.75	452.47	467.61
$C^d_{A2G}(\mathcal{E})$	−7.01	−5.41	58.23	668.18	650.02

Fig. 12 explains the rationale for the directionality of the sojourn time in the circular representation of the Von Mises distribution. The figure illustrates the circular distribution of street and building widths across the 72 metropolitan areas studied. The widths of the streets are greater than those of the buildings on the right side of the figure, which can be expressed as $w_s > w_b$where $-\frac{\pi}{2} \leq \mathcal{E} \leq \frac{\pi}{2}$.

6.5. Application: Offloading task size characterization

The connection of terrestrial users to airMECs with the best SINR yields the channel capacities for G2 A and A2G communication channels, as illustrated in Fig. 13, across both omnidirectional and directional scenarios. The estimation results of the environment-dependent communication channel capacity, as detailed in (14), (15), (16), and (17), are expressed in cubic polynomial form according to (36). The fitting parameters are provided in Table 7.

What is the maximum task size that can be offloaded without experiencing interruptions due to handover or signal loss? We conduct experiments to determine when the cumulative offloading delay surpasses the sojourn time. We employ environment-dependent channel

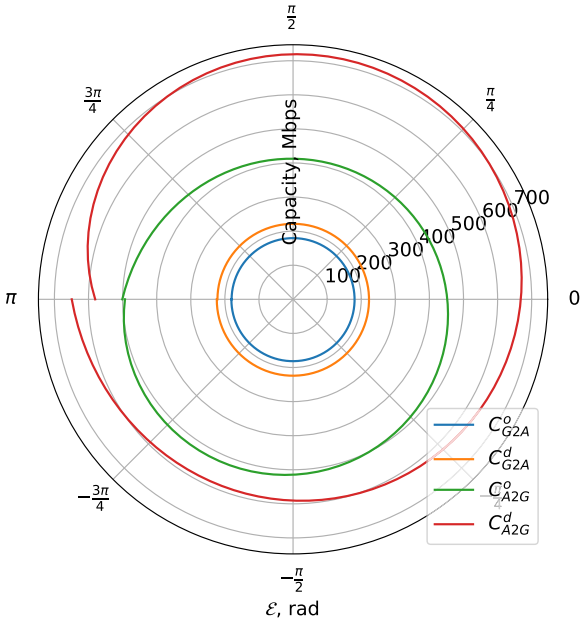

Fig. 13. The communication channel capacities for G2 A and A2G communication channels for omnidirectional and directional scenarios along the complex argument of urban layouts.

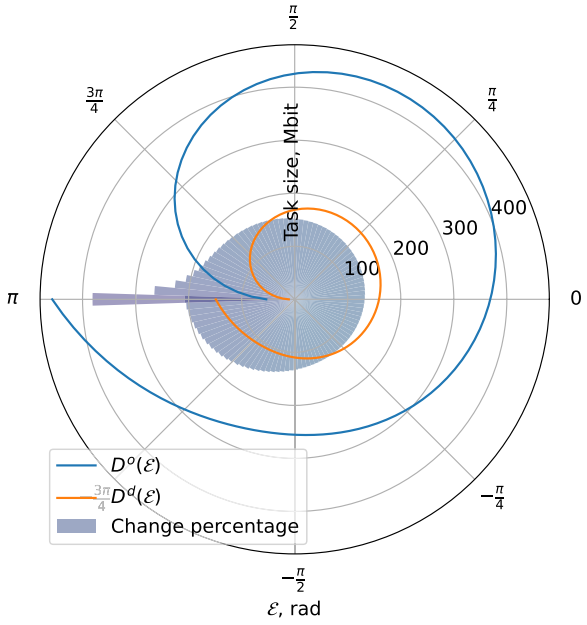

Fig. 14. Offloading task size as a function of $\mathcal{E}$ for omnidirectional and directional scenarios. The shaded bars represent the percentage difference between both scenarios.

capacity models, as detailed in Table 7, to determine the best upper limit of task size that may be offloaded from terrestrial users to airMECs during the interval between handovers. In each scenario, we randomly produce 1000 tasks. The task sizes are uniformly distributed between 5 Mbit and 250 Mbit in the directed scenario and between 5 Mbit and 500 Mbit in the omnidirectional case. The computational intensity is established at 1000 [cycle/bit], whereas the outcome of task computation in airMEC is determined to be 25 percent of the initial job size. The duration of task offloading is determined utilizing (24) and (25). The task size is established by identifying the point at which the offloading time nearly matches the sojourn duration for each unique environment.

Fig. 14 presents a polar representation of task size based on the urban environment for both omnidirectional and directed scenarios. The terms D^o and D^d represent the best upper limit for offloading workload size, contingent upon the complicated urban environment variable $\mathcal{E}$ in both omnidirectional and directional contexts, respectively. The shaded bar graph depicts the percentage change, computed using $100(D^o - D^d)/D^d$ [percent]. Despite the elevated G2 A and A2G channel capacities in the directional scenario, as seen in Fig. 13, the higher sojourn time of the omnidirectional scenario contributes to an average enhancement in task size of roughly 255 percent. The directional antenna configuration exhibits a 131 percent increase in capacity and a nearly equivalent percentage increase in SINR. This trade-off complicates the optimization of network capacity within the range $\mathcal{E} \in [-\pi, \frac{3\pi}{5}] \bigcup [\frac{3\pi}{4}, \pi]$, as the utilization of omnidirectional antennas may elevate interference, diminish SINR, and reduce channel capacity, whereas the deployment of directional antennas may improve SINR and channel capacity but concurrently escalate the handover rate in densely populated urban settings.

To examine this phenomenon thoroughly, we present two examples utilizing the four standard environments, as depicted in Figs. 15 and 16, which juxtapose the total task offloading time with the sojourn time across the four standard environments for omnidirectional and directional scenarios, respectively. The horizontal dotted lines indicate the intersection of task offloading time and sojourn time, hence, determining the task size. We employ $\mathcal{T}^o_{sinr}$ and $\mathcal{T}^d_{sinr}$ in both illustrations. Channel capacities are exponentially distributed using the obtained means from the models in Table 7. The reported results are the average

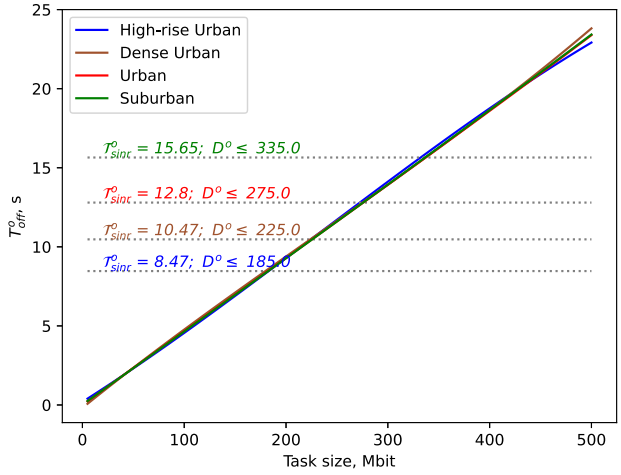

Fig. 15. An example of the task offloading time versus the task size is shown for the four standard urban environments in the omnidirectional scenario.

of ten samples. In Fig. 15, the average task sizes eligible for offloading in the four standard environments are 225, 185, 270, and 335 Mbit per environment sojourn time for dense urban, high-rise urban, urban, and suburban settings, respectively. In the directional context depicted in Fig. 16, the average task sizes eligible for offloading in the four standard environments are 74.29, 76.77, 153.48, and 210.4 [Mbit per environment sojourn time] for dense urban, high-rise urban, urban, and suburban settings, respectively. Although there is a linear relationship between job size and offloading time in both circumstances, the reduced sojourn time influenced the task size in the dense urban setting within the directional scenario.

Figs. 17 and 18 illustrate the influence of the environment-dependent sojourn time, as proposed in (36) and detailed in Table 5, on the cumulative task offloading time. We have established the job size at 100 Mbits and assessed channel capabilities using SINR-based connections. The colored bar plots in both images illustrate the disparity between sojourn and unloading times, indicating instances

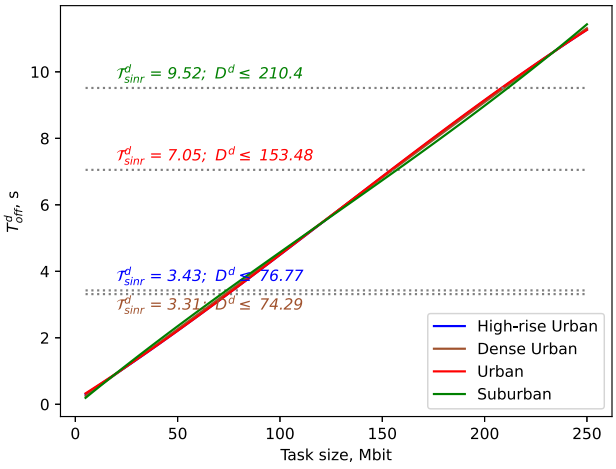

Fig. 16. An example of the task offloading time versus the task size is shown for the four standard urban environments in the directional scenario.

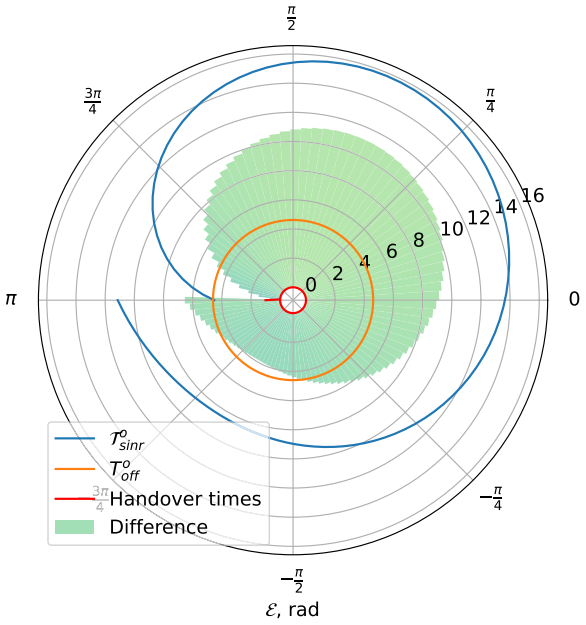

Fig. 17. Comparing the environment-dependent total offloading time of a task size $D_{i,j}$ = 100 Mbits with sojourn time $\mathcal{T}^o_{sinr}$. The red line shows the number of handovers during offloading, while the shaded bars represent the difference between $\mathcal{T}^o_{sinr}$ and T^o_{off}.

where offloading time surpasses sojourn duration. The quantity of handovers during task offloading is indicated in red and computed by taking the floor of the ratio of sojourn time to offloading time. Fig. 17 illustrates a single handover at $\mathcal{E} = \pi$, with an offloading time of 4.60 s and a sojourn time of 4.51 s. Fig. 18 illustrates an increased frequency of handovers during task offloading in the directional antenna context. The image illustrates handover inside a dense and high-rise metropolitan area, approximately within the range $\mathcal{E} \in (-\pi, -\frac{\pi}{2}] \bigcup [\frac{7\pi}{8}, \pi]$. For instance, when $\mathcal{E} = -\pi$, the handover happened four times, as seen by the red line in the polar plot. The mean number of handovers, dependent on the environment, is 0.37 throughout the whole range of $\mathcal{E}$; however, it is 1.16 inside the interval $\mathcal{E} \in (-\pi, -\frac{\pi}{2}] \bigcup [\frac{7\pi}{8}, \pi]$. If handover occurs during the offloading or before the result is sent back, the user might resend the task to the new serving airMEC, or the previous airMEC might migrate the result to the new serving airMEC,

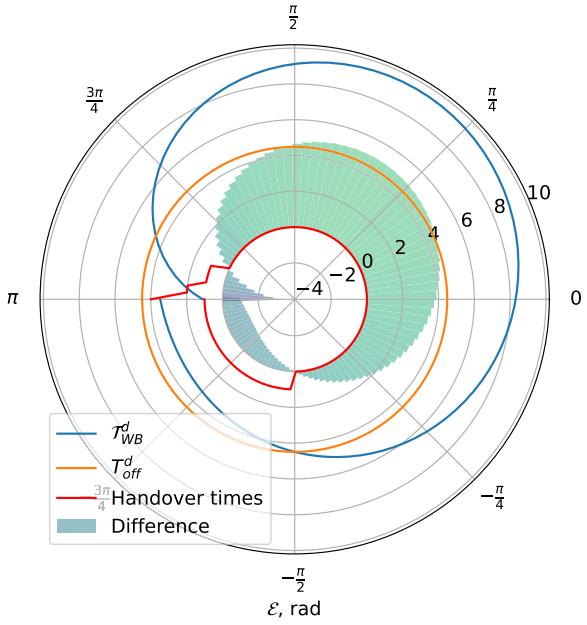

Fig. 18. Comparing the environment-dependent total offloading time of a task size $D_{i,j}$ = 100 Mbits with sojourn time $\mathcal{T}^d_{sinr}$. The red line shows the number of handovers during offloading, while the shaded bars represent the difference between $\mathcal{T}^d_{sinr}$ and T^d_{off}.

Table 8
Fitting parameters of the optimal upper limit of offloading task size.

Task size	a_i			
	0	1	2	3
$D^o(\mathcal{E})$	−16.0	−11.50	93.65	368.86
$D^d(\mathcal{E})$	−5.51	−8.01	32.42	159.06

which sends it back to the user. Both scenarios consume additional power; thus, controlling the task size based on the sojourn time will significantly enhance the overall power consumption.

We ultimately quantify the environment-dependent offloading task size using the expression in (36) and provide the fitting parameters in Table 8 for omnidirectional and directional antenna scenarios.

For real-time applications, several solutions can be introduced to minimize the computational time at airMECs, including but not limited to utilizing parallel processing, adopting acceleration technologies, employing predictive handover management, and adaptive task sizing. The task sizes and computational resources can be dimensioned in the planning phase to meet the environmental sojourn time. In the operational phase, optimization methods can employ mobility impact metrics like sojourn time to enhance the complexity. Moreover, the application's deadline constraint is not enough in urban environments. The offloading times in (24) and (25) must finish before any of the sojourn times or the application deadlines, as suggested in (38) and (39) for omnidirectional and directional scenarios.

$$T^o_{off}(\mathcal{E}, s_k) \leq \min(\mathcal{T}^o(\mathcal{E}), \tau_k), \forall \mathcal{E} \in [-\pi, \pi]. \tag{38}$$

$$T^d_{off}(\mathcal{E}, s_k) \leq \min(\mathcal{T}^d(\mathcal{E}), \tau_k), \forall \mathcal{E} \in [-\pi, \pi]. \tag{39}$$

7. Conclusion

The current literature has not sufficiently studied the joint effect of mobility and urban environments on data-intensive task offloading

from terrestrial users to airMECs. Focusing on large task sizes, we introduced a novel simplified circular representation of urban environments by extending the ITU-R P.1410 model. We propose statistical and analytical sojourn time approaches to quantify the combined effect of mobility and urban settings for omnidirectional and directional antenna scenarios. We simulate mobility in 72 urban configurations, first including buildings to quantify the statistical approach and then excluding buildings to validate the statistical results against the analytical model, while also measuring the influence of building existence. The results show 0.37 and 3.81 percent deviation between the statistical and analytical models for constant and dynamic velocities, respectively. The effect of buildings shows a decreased sojourn time of about 3.77 percent, while the circular analysis using Von Mises distribution shows a rotation of the probability concentration to the advantage of wider street environments. Finally, we use the proposed sojourn time to determine the maximum task sizes that we can offload during the handover intervals. The proposed models are not only improving resource dimensioning in the planning phase but also enhancing the optimization complexity during the operational phase.

This paper examines the prevalent SINR-based association of user–airMEC pairs, highlighting its inadequacy in representing the effects of urban environments. The development of channel models that depend on urban environments presents a promising avenue for future research. Additionally, quantifying the correlation between task size and task deadline within urban contexts is another significant area of inquiry. Furthermore, optimization methods based on sojourn time for task offloading to airMEC present a significant research opportunity that could contribute to the promised enhancement of the theoretical analysis of computational complexity.

CRediT authorship contribution statement

Basheer Ameen Raddwan: Writing – original draft, Visualization, Validation, Software, Resources, Methodology, Investigation, Formal analysis, Data curation, Conceptualization. **Ibrahim Ahmed Al-Baltah:** Writing – review & editing, Validation, Supervision, Project administration, Methodology.

Declaration of competing interest

The authors declare that they have no known competing financial interests or personal relationships that could have appeared to influence the work reported in this paper.

Appendix A. Urban configuration

For reproducibility, a list of parameters of the simulated 72 urban environments is presented in Table 9.

Appendix B. Supplementary data

Supplementary material related to this article can be found online at https://doi.org/10.1016/j.adhoc.2025.104019.

Data availability

I have shared the link to the research data.

UAV Mobility Tracing in 72 Urban Environments (Original data) (Mendeley Data)

Table 9
List of parameters of 72 urban environments.

α	β	γ	$\mathcal{E}$	α	β	γ	$\mathcal{E}$
0.41	100	36	−3.14	0.14	399	31	0.03
0.51	363	17	−3.05	0.19	283	33	0.07
0.65	633	12	−2.97	0.16	312	32	0.17
0.31	692	18	−2.88	0.16	668	21	0.28
0.76	329	22	−2.79	0.15	710	20	0.34
0.74	702	18	−2.7	0.1	634	20	0.46
0.72	319	31	−2.62	0.15	526	21	0.53
0.75	217	44	−2.53	0.12	201	31	0.61
0.47	579	26	−2.44	0.16	114	40	0.71
0.59	656	30	−2.36	0.12	625	14	0.78
0.59	392	44	−2.27	0.17	217	26	0.86
0.79	675	47	−2.18	0.13	232	16	0.96
0.49	621	40	−2.09	0.17	105	28	1.04
0.43	676	39	−2.01	0.19	149	23	1.15
0.33	511	37	−1.92	0.21	673	12	1.22
0.35	634	43	−1.84	0.24	359	23	1.31
0.29	479	42	−1.74	0.23	129	24	1.41
0.27	743	34	−1.66	0.24	649	10	1.49
0.25	661	23	−1.57	0.25	525	19	1.57
0.24	646	30	−1.49	0.26	588	10	1.65
0.19	735	47	−1.39	0.28	308	8	1.75
0.21	398	43	−1.31	0.28	387	12	1.81
0.18	586	41	−1.22	0.29	506	11	1.92
0.15	692	43	−1.16	0.3	274	15	2.01
0.2	422	36	−1.06	0.27	236	27	2.11
0.16	721	33	−0.96	0.32	695	9	2.16
0.16	293	49	−0.87	0.32	530	12	2.26
0.11	460	47	−0.79	0.33	236	18	2.36
0.13	477	40	−0.7	0.3	168	29	2.47
0.2	682	24	−0.61	0.38	287	13	2.53
0.15	447	35	−0.51	0.34	713	12	2.62
0.11	499	37	−0.44	0.43	494	9	2.71
0.1	566	34	−0.33	0.52	207	8	2.79
0.13	266	44	−0.27	0.51	473	8	2.89
0.15	428	32	−0.22	0.51	198	15	2.97
0.18	273	36	−0.13	0.56	532	9	3.05

References

[1] M. Chen, A. Liu, N.N. Xiong, Y. Ren, H.H. Song, ANNS: An intelligent advanced non-convex non-smooth scheme for IRS-aided next generation mobile communication networks, IEEE Trans. Mob. Comput. (2025) 1–14, http://dx.doi.org/10.1109/TMC.2025.3559099.

[2] B. Qiu, K. Feng, X. Li, H. Xiao, Z. Zhang, Mobility-aware user association and computation offloading in ultra-dense networks, IEEE Trans. Green Commun. Netw. (2025) 1, http://dx.doi.org/10.1109/TGCN.2025.3535766.

[3] S.K. uz Zaman, A.I. Jehangiri, T. Maqsood, Z. Ahmad, A.I. Umar, J. Shuja, E. Alanazi, W. Alasmary, Mobility-aware computational offloading in mobile edge networks: a survey, Clust. Comput. (2021) http://dx.doi.org/10.1007/s10586-021-03386-1.

[4] 3GPP TS 23.548, 5G system enhancements for edge computing, 2024.

[5] S.H. Alsamhi, A.V. Shvetsov, S. Kumar, J. Hassan, M.A. Alhartomi, S.V. Shvetsova, R. Sahal, A. Hawbani, Computing in the sky: A survey on intelligent ubiquitous computing for UAV-assisted 6G networks and industry 4.0/5.0, Drones 6 (7) (2022) http://dx.doi.org/10.3390/drones6070177.

[6] A.A. Baktayan, A. Thabit Zahary, I. Ahmed Al-Baltah, A systematic mapping study of UAV-enabled mobile edge computing for task offloading, IEEE Access 12 (2024) 101936–101970, http://dx.doi.org/10.1109/ACCESS.2024.3431922.

[7] M. Yan, R. Xiong, Y. Wang, C. Li, Edge computing task offloading optimization for a UAV-assisted internet of vehicles via deep reinforcement learning, IEEE Trans. Veh. Technol. 73 (4) (2024) 5647–5658, http://dx.doi.org/10.1109/TVT.2023.3331363.

[8] M.A. Saleem, S. Zhou, Z. Fengli, T. Ahmad, N. Nigar, M.U. Hadi, M. Shabaz, Delay, energy, and outage considerations in GenAI-Enhanced MEC-NOMA-enabled vehicular networks,, IEEE Trans. Intell. Transp. Syst. (2025) 1–15, http://dx.doi.org/10.1109/TITS.2025.3548268.

[9] Y. Liu, P. Lin, M. Zhang, Z. Zhang, F.R. Yu, Mobile-Aware Service Offloading for UAV-Assisted IoV: A Multiagent Tiny Distributed Learning Approach, IEEE Internet Things J. 11 (12) (2024) 21191–21201, http://dx.doi.org/10.1109/JIOT.2024.3373225.

[10] S.A. Zakaryia, M. Meaad, T. Nabil, M.K. Hussein, Task offloading and resource allocation for multi-UAV asset edge computing with multi-agent deep reinforcement learning, Computing 107 (5) (2025) 126, http://dx.doi.org/10.1007/s00607-025-01472-5.

[11] Z. Hashim Kareem, R. Qais Malik, S. Jawad, F. Abedi, Reinforcement Learning-Driven Task Offloading and Resource Allocation in Wireless IoT Networks, IEEE Access 13 (2025) 79314–79330, http://dx.doi.org/10.1109/ACCESS.2025.3563059.
[12] L. Li, P. Fan, Latency and Task Loss Probability for NOMA Assisted MEC in Mobility-Aware Vehicular Networks, IEEE Trans. Veh. Technol. 72 (5) (2023) 6891–6895, http://dx.doi.org/10.1109/TVT.2022.3233195.
[13] J. Zhang, H. Guo, J. Liu, Y. Zhang, Task Offloading in Vehicular Edge Computing Networks: A Load-Balancing Solution, IEEE Trans. Veh. Technol. 69 (2) (2020) 2092–2104, http://dx.doi.org/10.1109/TVT.2019.2959410.
[14] Y. Lu, Z. Chen, Q. Gao, T. Jing, J. Qian, A mobility-aware and sociality-associate computation offloading strategy for IoT, Wirel. Commun. Mob. Comput. 2021 (2021) 9919541, http://dx.doi.org/10.1155/2021/9919541.
[15] Y. Li, L. Li, P. Fan, Mobility-aware computation offloading and resource allocation for NOMA MEC in vehicular networks, IEEE Trans. Veh. Technol. 73 (8) (2024) 11934–11948, http://dx.doi.org/10.1109/TVT.2024.3375840.
[16] M. Mehrabi, S. Shen, Y. Hai, V. Latzko, G.P. Koudouridis, X. Gelabert, M. Reisslein, F.H.P. Fitzek, Mobility- and energy-aware cooperative edge offloading for dependent computation tasks, Network 1 (2) (2021) 191–214, http://dx.doi.org/10.3390/network1020012.
[17] S.S. Shinde, A. Bozorgchenani, D. Tarchi, Q. Ni, On the design of federated learning in latency and energy constrained computation offloading operations in vehicular edge computing systems, IEEE Trans. Veh. Technol. 71 (2) (2022) 2041–2057, http://dx.doi.org/10.1109/TVT.2021.3135332.
[18] H. Huang, W. Zhan, G. Min, Z. Duan, K. Peng, Mobility-aware computation offloading with load balancing in smart city networks using MEC federation, IEEE Trans. Mob. Comput. 23 (11) (2024) 10411–10428, http://dx.doi.org/10.1109/TMC.2024.3376377.
[19] B. Zhao, K. Peng, K. Zhang, H. Sun, Z. Tu, D. Chu, SerFlow: A Multistage Service-Enhanced Mechanism for Workflow Applications in CPSs With End-Edge–Cloud Collaboration, IEEE Internet Things J. 12 (16) (2025) 33792–33813, http://dx.doi.org/10.1109/JIOT.2025.3577233.
[20] P. q. Huang, Y. Wang, K. z. Wang, Energy-efficient trajectory planning for a multi-UAV-assisted mobile edge computing system, Front. Inf. Technol. Electron. Eng. 21 (12) (2020) 1713–1725, http://dx.doi.org/10.1631/FITEE.2000315.
[21] X. Qin, Z. Song, Y. Hao, X. Sun, Joint Resource Allocation and Trajectory Optimization for Multi-UAV-Assisted Multi-Access Mobile Edge Computing, IEEE Wirel. Commun. Lett. 10 (7) (2021) 1400–1404, http://dx.doi.org/10.1109/LWC.2021.3068793.
[22] Z. Liao, Y. Ma, J. Huang, J. Wang, J. Wang, HOTSPOT: A UAV-Assisted Dynamic Mobility-Aware Offloading for Mobile-Edge Computing in 3-D Space, IEEE Internet Things J. 8 (13) (2021) 10940–10952, http://dx.doi.org/10.1109/JIOT.2021.3051214.
[23] J. Ji, K. Zhu, C. Yi, D. Niyato, Energy Consumption Minimization in UAV-Assisted Mobile-Edge Computing Systems: Joint Resource Allocation and Trajectory Design, IEEE Internet Things J. 8 (10) (2021) 8570–8584, http://dx.doi.org/10.1109/JIOT.2020.3046788.
[24] M. Asim, W.K. Mashwani, S.B. Belhaouari, S. Hassan, A Novel Genetic Trajectory Planning Algorithm With Variable Population Size for Multi-UAV-Assisted Mobile Edge Computing System, IEEE Access 9 (2021) 125569–125579, http://dx.doi.org/10.1109/ACCESS.2021.3111318.
[25] L. Zhang, Z.-Y. Zhang, L. Min, C. Tang, H.-Y. Zhang, Y.-H. Wang, P. Cai, Task offloading and trajectory control for UAV-assisted mobile edge computing using deep reinforcement learning, IEEE Access 9 (2021) 53708–53719, http://dx.doi.org/10.1109/ACCESS.2021.3070908.
[26] D. Wei, J. Ma, L. Luo, Y. Wang, L. He, X. Li, Computation offloading over multi-UAV MEC network: A distributed deep reinforcement learning approach, Comput. Netw. 199 (2021) 108439, http://dx.doi.org/10.1016/j.comnet.2021.108439.
[27] Q. Wang, A. Gao, Y. Hu, Joint power and QoE optimization scheme for multi-UAV assisted offloading in mobile computing, IEEE Access 9 (2021) 21206–21217, http://dx.doi.org/10.1109/ACCESS.2021.3055335.
[28] B. Li, R. Yang, L. Liu, J. Wang, N. Zhang, M. Dong, Robust computation offloading and trajectory optimization for multi-UAV-assisted MEC: A multiagent DRL approach, IEEE Internet Things J. 11 (3) (2024) 4775–4786, http://dx.doi.org/10.1109/JIOT.2023.3300718.
[29] M. Ahmed, N. Fatima, S. Raza, H. Ali, A. Qayum, W. Ullah Khan, M. Sheraz, T. Chee Chuah, Optimizing resource allocation and task offloading in multi-UAV mec networks, IEEE Access 13 (2025) 68710–68725, http://dx.doi.org/10.1109/ACCESS.2025.3562102.
[30] ITU-RP Series, Recommendation ITU-R P.1410-6: Propagation Data and Prediction Methods Required for the Design of Terrestrial Broadband Radio Access Systems in a Frequency Range from 3 To 60 GHz, Tech. rep., 2023.
[31] B. Ameen Raddwan, I.A. Al-Baltah, Mobility-aware bivariate line-of-sight probability for air-to-ground communications using millimeter and terahertz waves, IEEE Access 13 (2025) 123913–123930, http://dx.doi.org/10.1109/ACCESS.2025.3582890.
[32] D. Wang, Z. Liu, X. Wang, Y. Lan, Mobility-aware task offloading and migration schemes in fog computing networks, IEEE Access 7 (2019) 43356–43368, http://dx.doi.org/10.1109/ACCESS.2019.2908263.
[33] X. Lin, R.K. Ganti, P.J. Fleming, J.G. Andrews, Towards understanding the fundamentals of mobility in cellular networks, IEEE Trans. Wirel. Commun. 12 (4) (2013) 1686–1698, http://dx.doi.org/10.1109/TWC.2013.022113.120506.
[34] M. Salehi, E. Hossain, Stochastic geometry analysis of sojourn time in multi-tier cellular networks, IEEE Trans. Wirel. Commun. 20 (3) (2021) 1816–1830, http://dx.doi.org/10.1109/TWC.2020.3036894.
[35] M. Salehi, E. Hossain, Handover rate and sojourn time analysis in mobile drone-assisted cellular networks, IEEE Wirel. Commun. Lett. 10 (2) (2021) 392–395, http://dx.doi.org/10.1109/LWC.2020.3032596.
[36] B. Raddwan, I.A. Al-Baltah, Line-of-sight probability models for 5G/6G millimeter-wave networks: A review, Sana'A Univ. J. Appl. Sci. Technol. 2 (5) (2024) 440–452, http://dx.doi.org/10.59628/jast.v2i5.1054.
[37] B.A. Raddwan, I. Ahmed Al-Baltah, M. Ghaleb, Environment-aware 3D mobility simulation for the 5G and 6G wireless networks, in: 2024 1st International Conference on Emerging Technologies for Dependable Internet of Things, ICETI, 2024, pp. 1–8, http://dx.doi.org/10.1109/ICETI63946.2024.10777167.
[38] I. Mohammed, S. Gopalam, I.B. Collings, S.V. Hanly, Closed form approximations for UAV line-of-sight probability in urban environments, IEEE Access 11 (2023) 40162–40174, http://dx.doi.org/10.1109/ACCESS.2023.3267808.
[39] A. Saboor, E. Vinogradov, Z. Cui, A. Al-Hourani, S. Pollin, A geometry-based modelling approach for the line-of-sight probability in UAV communications, IEEE Open J. Commun. Soc. 5 (2024) 364–378, http://dx.doi.org/10.1109/OJCOMS.2023.3341627.
[40] 3GPPTR 38.900 - V14.2.0, Study on Channel Model for Frequency Spectrum above 6 GHz, Tech. rep., 2017.
[41] M. Abramowitz, I. Stegun, Handbook of Mathematical Functions with Formulas, Graphs, and Mathematical Tables, Vol. 55, National Bureau of Standards Applied Mathematics Series, 1972.
[42] B. Raddwan, UAV mobility tracing in 72 urban environments, 2025, http://dx.doi.org/10.17632/tggb5kvj6s.1.

Basheer Ameen Raddwan received his B.Sc. degree in electrical and electronic engineering, majoring in telecommunication, in 2003 from Sana'a University, Yemen. Since then, he has worked for Yemen Mobile Company as a manager of core network planning. He received his M.Sc. degree in information technology in 2019 from the University of Modern Sciences in Sana'a, Yemen. He is a Ph.D. student at Sana'a University in Yemen. He focused on the virtualization of mobile core network functions, migration to network function virtualization architecture, and the next generation of mobile networks. He built several private cloud systems that use mainstream systems, such as Ceph storage, OpenStack, and Kubernetes.

Ibrahim Ahmed Al-Baltah received the B.Sc. degree in statistics and computer science from the University of Gezira, Sudan, in 2007, and the M.Sc. and Ph.D. degrees in software engineering from University Putra Malaysia, Malaysia, in 2009 and 2014, respectively. He is currently an Associate Professor with the Department of Information Technology, Sana'a University, where he has been a Faculty Member, since 2015. He is also the Head of the Information Technology Department. His research interests include green software engineering, resilience software engineering, cognitive software engineering, semantic web, semantic web of things, and semantic data fusion.